

Original Article

Cite this article: Tripathi S and Deb M. Decoding imprints of hydrothermal alteration around Imalia polymetallic sulphide deposit, Central Indian Tectonic Zone, and its implications on ore genesis. *Geological Magazine* 162(e12): 1–27. <https://doi.org/10.1017/S0016756825000056>

Received: 30 August 2024

Revised: 17 February 2025

Accepted: 26 February 2025

Keywords:

Imalia; Mahakoshal belt; Hydrothermal alteration; Chlorite; Brittle zone

Corresponding author:

Shubham Tripathi; Email: stripathi@live.in

Decoding imprints of hydrothermal alteration around Imalia polymetallic sulphide deposit, Central Indian Tectonic Zone, and its implications on ore genesis.

Shubham Tripathi  and Mihir Deb 

Department of Geology, University of Delhi, Delhi 110007, India

Abstract

The Imalia polyphase polymetallic deposit, located in the Mahakoshal belt of Central India, is hosted by carbonate rocks. The major part of mineralisation at Imalia results from hydrothermal activity induced by the intrusion of quartz porphyry dykes, which also formed an alteration halo of silicate and oxide minerals during their interaction with the host lithology. The initial silicates to form were hydrothermal Ca-amphibole and a minor amount of garnet, followed by potassic phases including biotite and K-feldspar, as well as rutile, apatite, titanite, pyrite, magnetite and rare calcite and ilmenite. A subsequent, cooler pulse of hydrothermal fluid overprinted the earlier-formed silicates and was responsible for the bulk of the sulphide mineralisation at Imalia. During this transformation phase, propylitic silicates primarily consisting of chlorite and epidote, along with a modest proportion of actinolite, albite, titanite, sericite and calcite, formed, accompanied by iron-rich oxide phases including magnetite, hematite and ilmenite. These silicates mostly formed under high water-to-rock ratios with significant meteoric water influence. Geothermometric and fluid inclusion data indicate that alteration zone minerals formed at temperatures between approximately 150°C and 550°C, at pressures of around 1 kbar and depths of less than 10 km, with a mean oxygen fugacity of $\log f_{O_2} -32$, closely aligned with the FMQ buffer. The alteration zone minerals record the evolution of hydrothermal fluids in a predominantly brittle structural regime, characterised by episodic decompression due to fluid overpressuring and hydrofracturing, as evidenced by various types of breccias, diverse quartz veins, open space-filling textures and fluid inclusion data.

1. Introduction

A large number of ore deposits are generated by hydrothermal solutions. Hydrothermal ore deposits form when a hot, aqueous solution carrying metals and other components precipitates minerals in ore traps due to physico-chemical disequilibrium between rocks and fluid (Skinner 1997). This disequilibrium initiates a process known as hydrothermal alteration, where a chemical replacement of original minerals in a rock by new minerals occurs. During alteration, the hydrothermal fluid delivers chemical reactants and removes aqueous reaction products. The process is influenced by variations in temperature, pressure and, most importantly, fluid composition (Reed, 1997; Rose and Burt, 1979). During hydrothermal alteration, a variety of minerals form, often displaying a wide range of chemical compositions and subtypes that reflect the diverse physico-chemical conditions under which they precipitated. For example, chlorite, a common mineral in hydrothermal alteration zones, exhibits a broad range of chemical compositions. This variability may relate to the compositions of the minerals it replaces, the nature of the hydrothermal fluids from which it precipitated, and the temperatures at which it formed (from 40°C to 600°C) (Beaufort *et al.* 2015; Xiao and Huayong, 2020). Due to its non-stoichiometric nature, chlorite records valuable information about the conditions during fluid-rock interaction events that contribute to ore-forming processes. Understanding hydrothermal alteration, therefore, provides important insights into the chemical attributes and origins of ore fluids and the physical conditions of ore formation (Beane and Titley, 1981; Henley, 1985; Reed, 1997; Pirajno, 2009 and references therein). Moreover, in most mineral deposits, hydrothermal alteration assemblages display zonal patterns that reflect progressive rock buffering from the ore zone to the least altered host rock (Ronghua *et al.* 2002; Inoue, 1995; Lobato *et al.* 1998). Consequently, understanding alteration halos is crucial for setting exploration targets in prospective zones for mineral deposits.

The Mahakoshal Supracrustal Belt (MSB) in central India has been a major target for exploration agencies, particularly the Geological Survey of India (GSI), in the search for new noble metal deposits to meet the rising domestic demand. Thanks to their continuous efforts, several deposits have been identified in both the eastern and western parts of the Mahakoshal

© The Author(s), 2025. Published by Cambridge University Press. This is an Open Access article, distributed under the terms of the Creative Commons Attribution licence (<https://creativecommons.org/licenses/by/4.0/>), which permits unrestricted re-use, distribution and reproduction, provided the original article is properly cited.



Belt. In the eastern part, prominent deposits include Gurhar Pahar, Chakaria and Gulaldih. In the western part, the main Au deposits identified are at Imalia, Barhi, Jhal, Selarpur and Vilayat Kalan (Devarajan *et al.* 1998, Talusani, 2001). Among them, Imalia stands out as a unique and important polymetallic deposit, hosting a range of metals including Pb, Zn, Cu, Au, Ag, Sn, W, Mo, In and Se. Recently, Tripathi and Deb (2022) published a detailed account of the unique mineralogy and rare phases present in the Imalia deposit. Most of the mineralisation at Imalia has been attributed to hydrothermal activity induced by the intrusion of quartz porphyry dykes (Singhai and Singh, 2001; Tripathi, 2008). This hydrothermal activity also created an alteration halo, where several minerals formed during the interaction of the hydrothermal fluid with the host lithology. These minerals record the chemical characteristics of the hydrothermal fluid and provide important clues for mass transfer during hydrothermal fluid advection. The present study thus focuses on the distribution patterns, textural relationships and chemical composition of the main hydrothermal minerals in the alteration zone of the Imalia deposit.

2. Geological background

2.a. Regional setting

Presenting the first cogent synthesis of the plate tectonic evolution of Precambrian ‘terranes’ of the Indian shield, Radhakrishna (1989) proposed a ‘Central Indian Tectonic Zone’ (CITZ) marking the junction of the Bundelkhand block in the north and the Peninsular block in the south, later envisaged by Yedekar *et al.* 1990 as two proto-continents separated in mid- to late Archean by a narrow intercratonic basin. The ENE-WSW trending MSB is a prominent asymmetrical rift basin in the northern part of CITZ, the northern and southern boundaries of which are marked by crustal-scale faults, specifically the Son-Narmada North Fault (SNNF) and the Son-Narmada South Fault (SNSF) (Roy and Prasad, 2003) (Figure 1). The rocks of MSB have experienced polyphase tectonothermal events involving several cycles of volcano-sedimentary deposition, deformation, metamorphism and magmatism and are endowed with a number of ore deposits, including the one at Imalia. The lithology of the MSB comprises quartzite, phyllite, carbonate, chert, banded iron formation (BIF), greywacke, argillite, polymictic conglomerate, along with basic metavolcanics, pyroclastics, ultramafics, granitoids, syenite, lamp-phyres, mafic dykes and a range of alkaline intrusives (Acharyya and Roy, 2000; Roy and Prasad, 2003; Roy and Bandyopadhyay, 1990; Bora and Kumar, 2015). Based on these lithological characteristics, Nair *et al.* (1995) referred to MSB as a Proterozoic greenstone belt. Roy and Devarajan (2000) grouped these litho-assemblages into three formations, in ascending stratigraphic order: Sleemanabad, Parsoi and Dudhamaniya, intruded by igneous rocks. These formations exhibit markedly different spatial distributions in the Mahakoshal belt. The Dudhamaniya Formation is more prominent in the eastern part, while the Sleemanabad Formation, which hosts the mineralisation at Imalia, is widespread in the western part. The Sleemanabad Formation is represented by carbonate rocks with bands of bedded and massive chert, BIF, rare banded magnetite-rich chert, quartz arenite, thin bands of argillites and metavolcanic rocks (Figure 2). The Mahakoshal supracrustals have undergone three phases of deformation and are characterised by regional greenschist facies metamorphism (Nair *et al.* 1995; Roy and Bandyopadhyay, 1990)

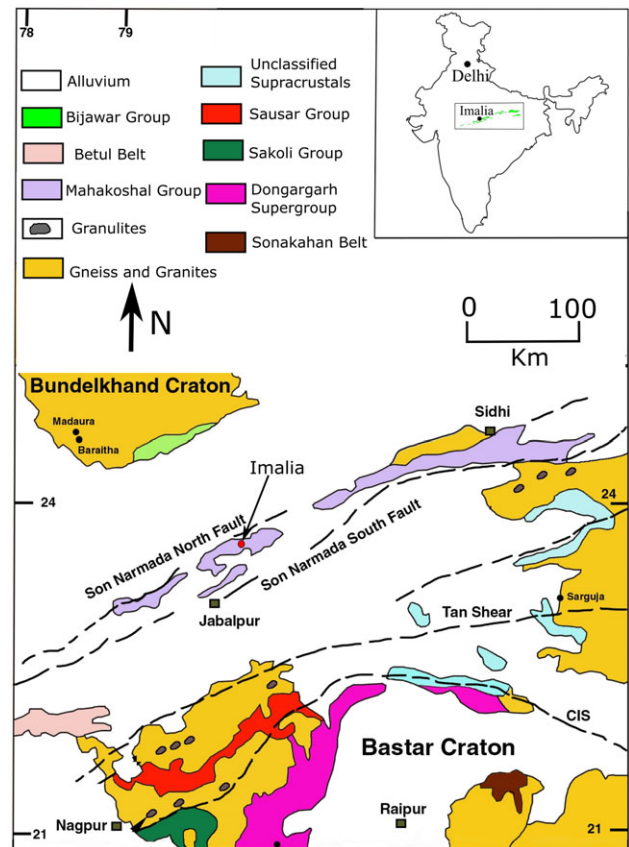


Figure 1. Geological map of central India showing supracrustal belts and shear zones (modified after Roy and Prasad, 2003), defining the Central Indian Tectonic Zone (CITZ). The Mahakoshal Group is part of the Proterozoic belt. Abbreviation: CIS – Central Indian Suture.

and syn- to post tectonic granitic and alkalic intrusions (Roy and Devarajan, 2000) (cf. Figure 2 and Tripathi and Deb, 2022 for more information on these features). Geochronological data for these rocks are sparse, but a Paleoproterozoic age of MSB is still evident. The granites intruding into MSB yielded an Rb–Sr age of 1800–1700 Ma (Roy and Devarajan, 2000). More recently, Deshmukh *et al.* (2017) suggested age constraints for different metamorphic stages based on U–Th–total Pb monazite age dating of pelitic schists and phyllites from the eastern Mahakoshal belt: M1 (prograde) 1800–1900 Ma, M2 (peak) 1650–1750 Ma and M3 (retrograde) 1500–1600 Ma, broadly synchronous with granitoid intrusions. In a recent publication, Sharma *et al.* (2022) recorded a crystallisation and deposition age of 1894.3 ± 9.4 Ma for the dacitic to rhyolitic pyroclastic unit of the Parsoi Formation in the eastern Mahakoshal belt. Earlier Pb–Pb model ages of approximately 2050 Ma were estimated for Pb–Zn sulphides (Tripathi, 2008) hosted by the carbonates of the Sleemanabad Formation at Imalia; this represents one of the oldest age data available from the western Mahakoshal belt.

2.b. Geological setting of Imalia deposit

In the Sleemanabad area where the Imalia deposit is located (Figure 2), Mahakoshal group of rocks is stratigraphically represented by the lower Sleemanabad Formation, followed by the upper Parsoi Formation. The lower Sleemanabad Formation

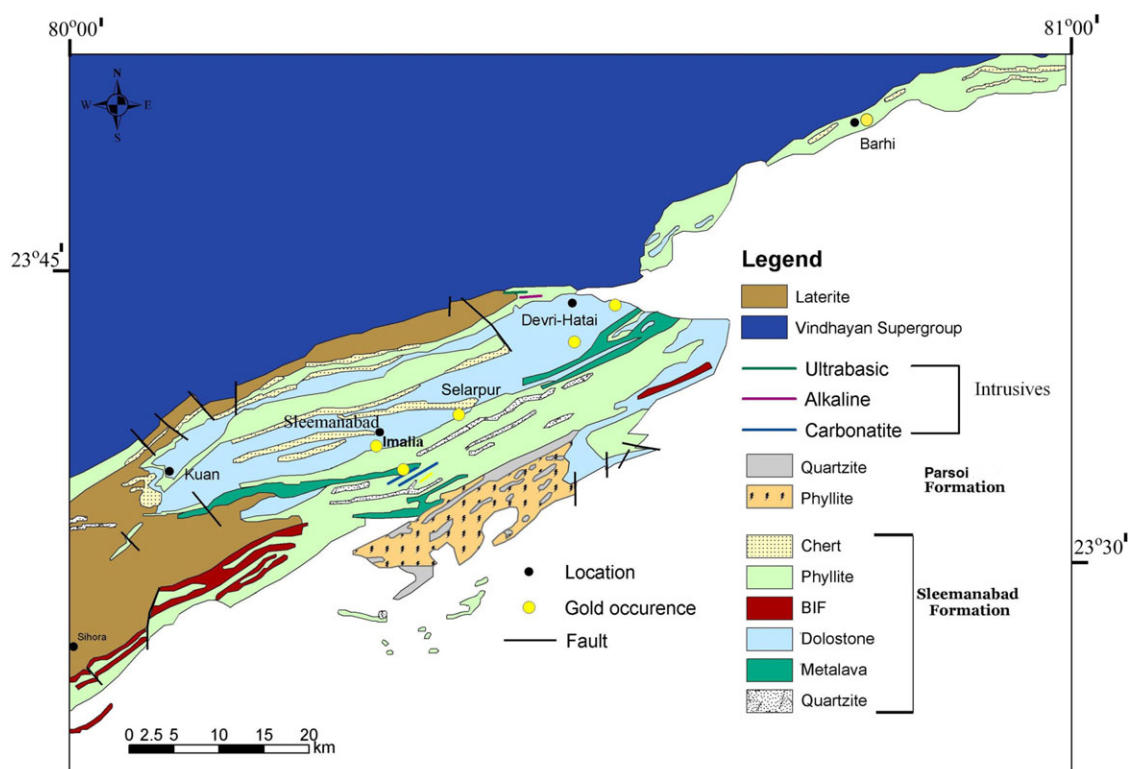


Figure 2. Geological map of Western Mahakoshal belt. (modified after Mineral Atlas of India, Geological Survey of India, 2001.)

consists of basal quartzites overlain by a thick sequence of dolostone with chert interbeds. This formation also includes dolostones interbedded with metavolcanic rocks and phyllites, with a few quartzite bands. The upper Parsoi Formation is mainly composed of quartzites and phyllites, with a thin conglomerate band at its base.

The lithology in the Imalia ore zone is mainly recrystallised dolostone from the Sleemanabad Formation (Figure 2). These dolostones are intercalated with thin bands of buff-coloured phyllite, greyish chert and jasper. The bedding trend of the dolostones in all studied outcrops is ENE-WSW. Three phases of deformation are noted in these rocks. The F1 folds are tight, isoclinal folds with vertical or steeply southerly dipping axial planes, and their axes trend ENE-WSW. The second phase, F2, has folded the axial plane of F1, resulting in only mesoscopic folds in some areas. The axial plane of the F2 folds dips steeply to the north. F3 folds, formed in the third phase of deformation, are not very prominent and appear as open warps with N-S axes. The carbonate rocks at Imalia exhibit localised brecciation and several sets of fractures, some of which are filled with later quartz veins showing a comb texture. Additionally, carbonate breccia was observed in some outcrops. The carbonate rocks occasionally include interbeds of jasper and light greenish to grey chert. Rare outcrops of dolostone with phyllitic intercalations are also present. The general strike of foliation in phyllite is N65°E–S65°W, dipping 70° to the southeast. Quartz porphyry dykes trending NNW–SSE to N–S are an important igneous lithology observed in numerous outcrops at Imalia. Kaolinization is noted along fractures and joint planes of the quartz porphyry dykes. Fluorite, pyrite and rare magnetite

appear as specks and disseminations and are also found along shear planes developed along the margins of the intrusions. Regionally, a few outcrops of meta-mafic lava and small basic dykes have been identified (Tripathi, 2008; GSI unpublished report).

2.c. Nature of the mineralisation

Exploration activities over a protracted period in the last few decades, mainly drilling conducted by the Geological Survey of India (GSI), have helped identify two main N–S trending and one minor north-west trending mineralised zones in Imalia. The two main mineralised zones, eastern and the western, are confined to fractures and shears in the recrystallised dolostone, roughly conforming to the trend of the quartz porphyry dykes (Figure 3). The longest and most promising eastern zone extends for about 750 metres. Surface indications of this mineralisation, including gossans and oxidised zone, and earlier workings such as pits, trenches and shafts, as well as the metal (Au, Ag, Pb, Zn, Cu, Sn) abundances in these ore zones have been described in detail by Tripathi and Deb (2022). Only the background information regarding the nature of the mineralisation, relevant to this study, is presented here.

Surface exposures in the area are sporadic, and with no current mining activity, borehole cores (partially preserved over specific lengths) provided by GSI formed the basis of the present study. Core logging of 30 boreholes was carried out, but complete core lengths were only available for a few (see Figures 4a, b, c). Detailed core logging of all available cores, followed by ore petrologic studies, helped identify the nature of mineralisation and different

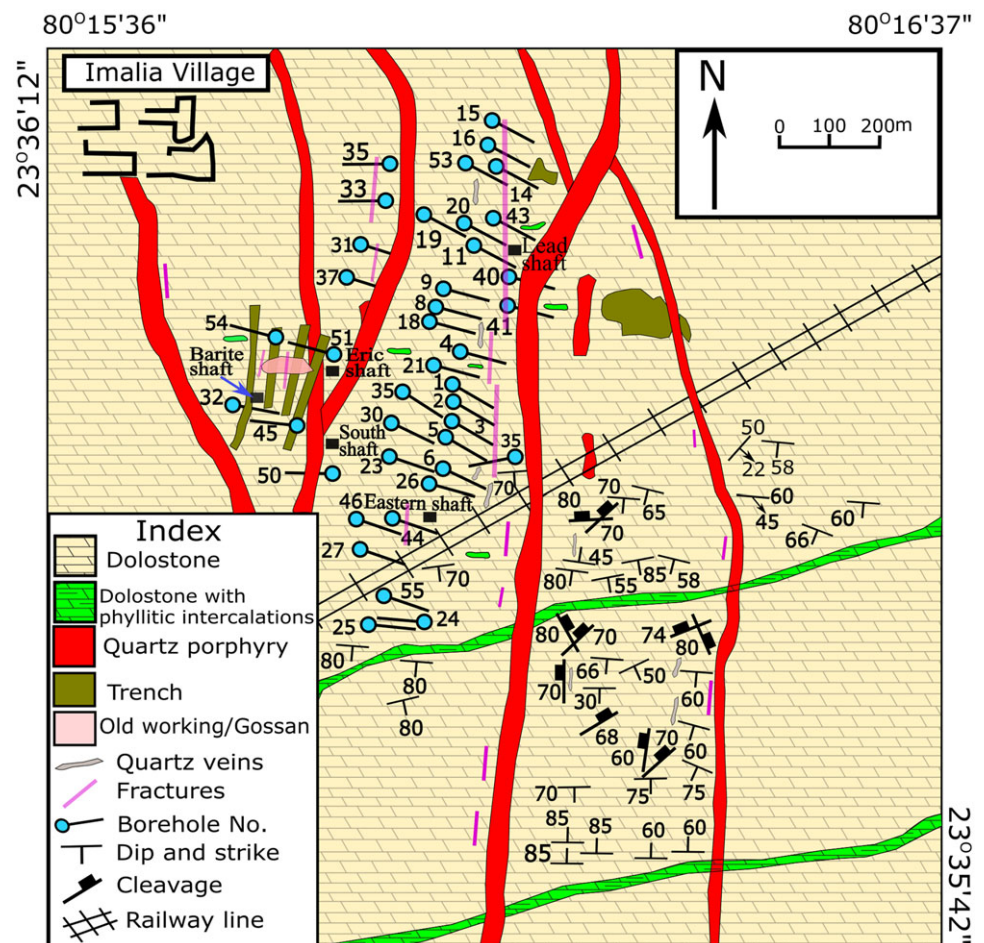


Figure 3. Geological map of Imalia deposit, Mahakoshal belt, Central India, showing drill holes and surface extrapolation of quartz porphyry dykes and other litho-units based on drill hole and surface data (modified after GSI unpublished map).

ore types at Imalia (Tripathi and Deb, 2022), which are listed below (referred to by their numbers in the following text):

- 1) Sporadic pyrite crystals in dolostones, of diagenetic affiliation.
- 2) Galena-sphalerite-rich sulphide ores occurring as irregular patches, stringers, streaks or blebs, and veinlets in recrystallised dolostone. Also found segregated along foliation planes, fractures, and joint planes in silicified dolostones.
- 3) Disseminated magnetite in chlorite \pm epidote-rich recrystallised dolostone.
- 4) Pyrite-arsenopyrite ores, showing the following variations:
 - (a) Disseminated and evenly distributed, mainly in dolostone and also in phyllitic intercalated dolostone, occurring parallel to primary stratification or as fine disseminations filling intergranular spaces.
 - (b) Pyrite-rich veins in recrystallised dolostone.
 - (c) Massive pyrite-arsenopyrite ore. Massive lenses of sulphides have been intersected in drill holes mostly along the axial planes of cross folds (GSI, unpublished report).

As mentioned earlier, the Pb-Pb dating of the galena from type 2 ore from Imalia yielded 2050 Ma of age, representing a small but first significant mineralisation event in Imalia (Tripathi, 2008). This ore type consisted of network to massive Pb-Zn sulphide ores with pervasive metamorphic textures (Tripathi and Deb, 2022)

formed during the regional metamorphism of the Mahakoshal belt. Type 3 and type 4 ore, which constitute the bulk of the mineralisation at Imalia, formed later at approximately 1700 Ma, as deduced from the U-Pb dating of the porphyry dykes at Imalia (Tripathi and Deb unpublished data). The present work covers a detailed account of the alteration halo formed in the course of the emplacement of vein-type mineralisation (types 3 and 4) in Imalia.

3. Materials and methods

This study of hydrothermal alteration in Imalia deposit was based primarily on drill core samples, as surface exposures of the litho-units were rather limited. Following detailed logging of the available drill cores, representative specimens were collected and approximately 50 polished thin sections and epoxy mounts were prepared. Petrographic studies were conducted under reflected and transmitted light using a petrological microscope for mineralogical and textural observations, and under an electron microprobe for their mineral chemistry. The EPMA work was conducted at GSI lab in Faridabad, using a Cameca SX-50 electron microprobe analyser. For silicate analyses, operating conditions were set at 15 kV voltage, 12 nA probe current and a 1 μ m beam diameter, with various natural and synthetic minerals serving as standards. PAP corrections (Pouchou and Pichoir, 1988) were applied to the raw data. Additional microprobe analyses were conducted at the

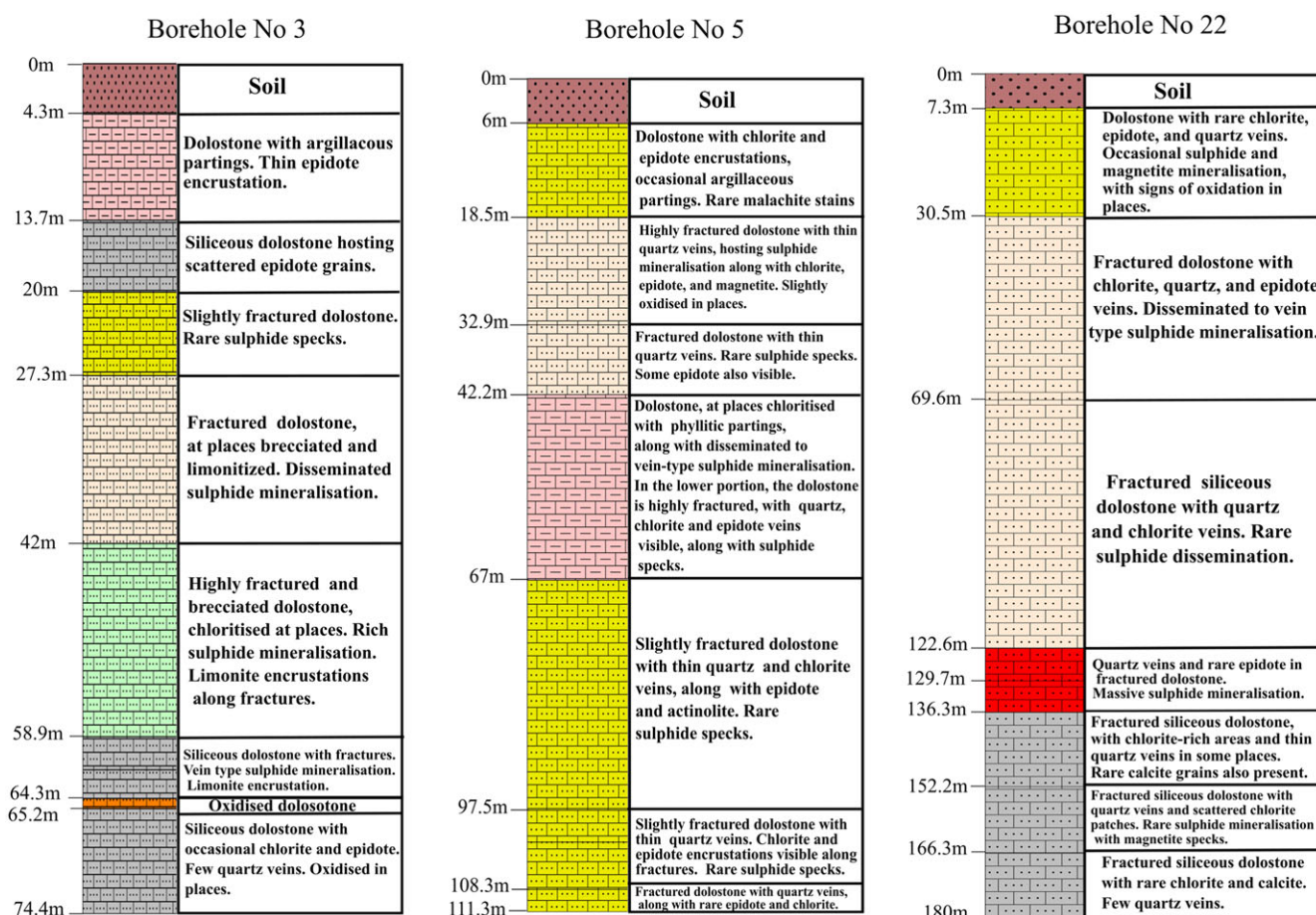


Figure 4. Drill core logs of borehole No. 3, 5 and 22 showing the lithological variation in the mineralised zone of the Imalia deposit.

National Centre for Experimental Mineralogy and Petrology, University of Allahabad, using a JEOL JXA 8100 electron probe X-ray microanalyser equipped with a 3-channel wavelength dispersive spectrometer (WDS). These analyses employed conditions of 15 kV voltage, 20 nA probe current and a 2 μm beam diameter. Multi-mineral standards were used, and ZAF corrections for X-ray absorption, atomic number effect, backscatter and ionisation penetration losses were applied to the raw data using the instrument's software. Mineral chemical data for the major oxides (in weight percent) were obtained from the microprobe analysis and converted to cations per formula unit via a Microsoft Excel program based on the procedure of Deer *et al.* (1992).

The fluid inclusion study of Imalia ore samples was challenging due to the small size of inclusions in the associated quartz/carbonate grains. Despite these challenges, wafers from representative samples of type 3 and type 4 ore were prepared, but only a very limited number of determinations were possible. For the fluid inclusion study first wafers were observed under a conventional petrological microscope to determine in the host quartz/carbonate grains the number of phases, degree of fill, size, genetic type (primary, pseudo-secondary and secondary) of fluid inclusions and their relationship to mineralisation (Shepherd *et al.* 1985; Bodnar *et al.* 1985; Bodnar *et al.* 2014). Heating runs were performed using a Linkam THMS 600 heating-freezing unit attached to a Leica DMRL petrological microscope to determine the melting temperatures of ice [Tm(ice)] and CO₂ [Tm(CO₂)], the homogenisation temperature of CO₂

[Th(CO₂)] and the total homogenisation temperature [Th]. Repeated freezing and heating runs on selected inclusions showed freezing temperatures reproducible within $\pm 0.5^\circ\text{C}$ and homogenisation temperatures within $\pm 0.4^\circ\text{C}$.

4. Results

4.a. Petrologic characteristics of hydrothermal alteration

Recrystallised dolostone, at some places showing intercalations of phyllite, is the main host of Imalia deposit. Quartz porphyry rock, in the form of dykes, is another conspicuous lithology in the mineralised zone (Figure 3). The intrusion of porphyry dykes in the Imalia area initiated the generation of hot magmatic-hydrothermal fluids that began interacting with the carbonate host lithology. This interaction created an alteration halo mainly consisting of chlorite, epidote and magnetite-rich zones, referred to as type 3 ore in this study, which was subsequently followed by vein-type mineralisation (type 4 ore). The diagenetic pyrite (type 1 ore) and Pb–Zn mineralisation (type 2 ore) predate the vein-type mineralisation (Tripathi, 2008). A small amount of these alteration halo minerals is also observed in a few samples hosting the earlier mineralisation. This is likely due to spatial proximity of the earlier mineralisation with type 3 and type 4 ores. The hydrothermal alteration in Imalia appears to be pervasive and can be broadly categorised into potassic, propylitic, phyllic and argillic alteration.

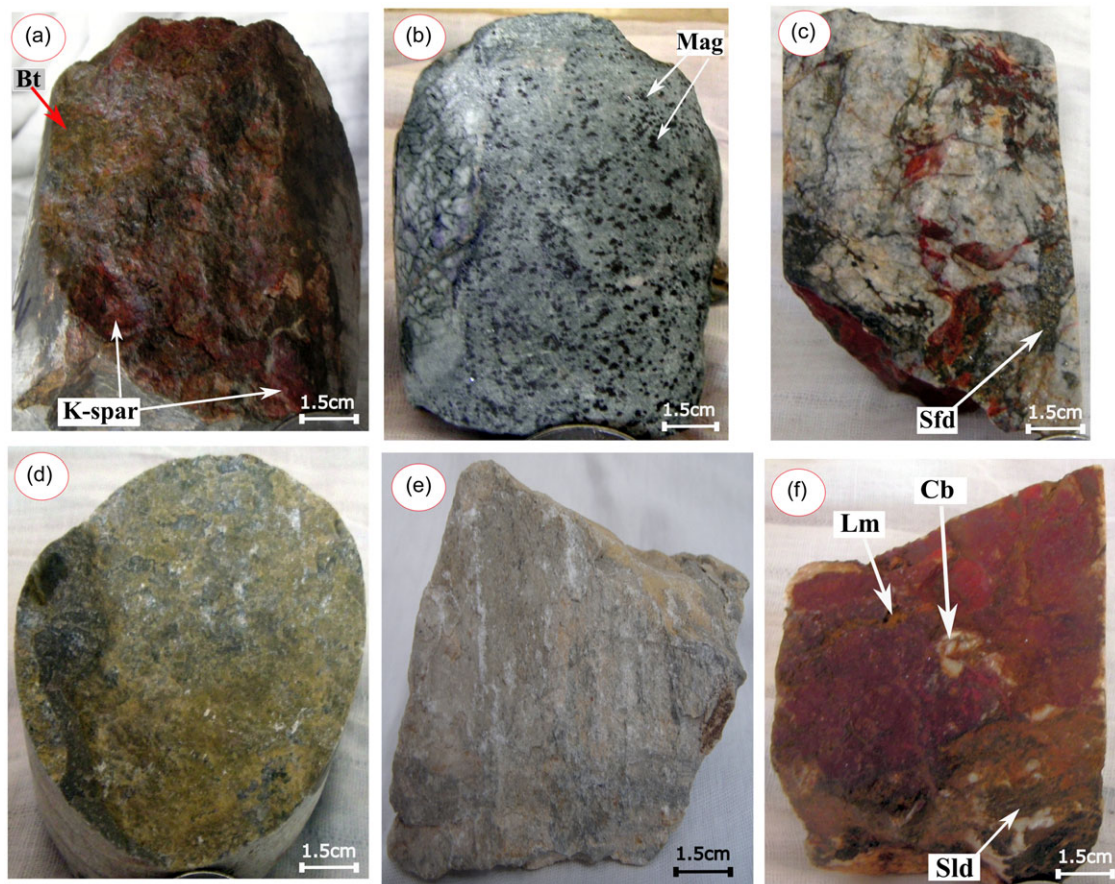


Figure 5. Hand specimen samples showing the characteristic features of the alteration zone from the Imalia deposit. (a) Biotite and K-feldspar rich sample from the potassic zone. (b) Chloritised dolostone with disseminated magnetite grains. (c) Chlorite veins in the recrystallised dolostone, along with disseminated sulphides. (d) Epidote-rich recrystallised dolostone. (e) Sericitised sample from the phyllic zone. (f) Bright red jasper sample formed by replacing the host carbonate, with visible sulphide disseminations and localised limonitization. Abbreviations: K-spar – K-feldspar, Mag – Magnetite, Sld – Sulphide, Lm – Limonite, Cb – Carbonate, Bt- Biotite.

These alterations are responsible for the compositional transformation of the dolostone wall rocks to various degrees, resulting in the formation of silicified dolostone and impure marble. Although the intensity of the different types of alteration varies in Imalia, a consistent paragenetic sequence of alteration can be discerned based on the textural characteristics and spatial distribution of the minerals in the mineralised zone.

A small amount of amphibole and rare garnet grains appear to be the initial products of the interaction between high-temperature hydrothermal fluids and the carbonate host rocks (Figures 6a, b). This was followed by the precipitation of a sizable concentration of potassic minerals in the ore zone, mainly biotite and K-feldspar (Figures 5a, 6c, d), along with smaller amounts of quartz, apatite, rutile, pyrite, rare titanite, calcite and ilmenite (Figures 6d, e). Biotite also appears to be replacing earlier precipitated amphibole in some places (Figure 6a). Magnetite grains were observed in the potassic domain, marking the onset of iron oxide precipitation within the alteration sequence. Mesoscopic and microscopic petrographic evidence suggests that later propylitic alteration overprinted the earlier potassic alteration, leaving only traces of its presence in the Imalia alteration zone.

Chloritization marks the most widespread and pervasive propylitic alteration in the Imalia deposit, forming a proximal halo around the main orebodies, as observed in borehole studies (Figures 4a, b, c). Chlorite forms dense networks of crosscutting

veinlets and fine-grained to massive aggregates that completely overprint earlier alterations and, in places, completely replace the host rocks (Figures 5b, c). In many studied sections, chlorite appears to be closely associated with earlier precipitated biotite. Based on petrographic evidence, this secondary chlorite can be grouped into two broad categories: 1) chlorite (Chl1), which is a product of direct precipitation from hydrothermal fluid (Figure 6f); and 2) chlorite (Chl2), formed by the replacement of biotite (Figures 6g, h). The latter appears to replace biotite along the edges of the grain and also displays pseudomorphism, preserving the original shape of the biotite grain during the alteration process. Epidote, another important silicate mineral, is present in significant amounts in the propylitic zone along with chlorite (Figures 5d and 7a, b). Borehole data and petrographic studies indicate that epidote was more abundant in the proximal part of the mineralisation and also replaces earlier precipitated biotite in some samples. Actinolite, albite, titanite, calcite and rare rutile are also present in small amounts in the propylitic zone (Figures 7a, b, c). Both chlorite and epidote variably replace actinolite in a number of samples.

Since carbonate rocks constitute the main wall rock in the Imalia area, they underwent significant compositional changes during the hydrothermal surge. Compositional data indicate that dolomitization of the carbonates occurred on a regional scale prior to mineralisation (Tripathi, 2008). Hydrothermal fluids

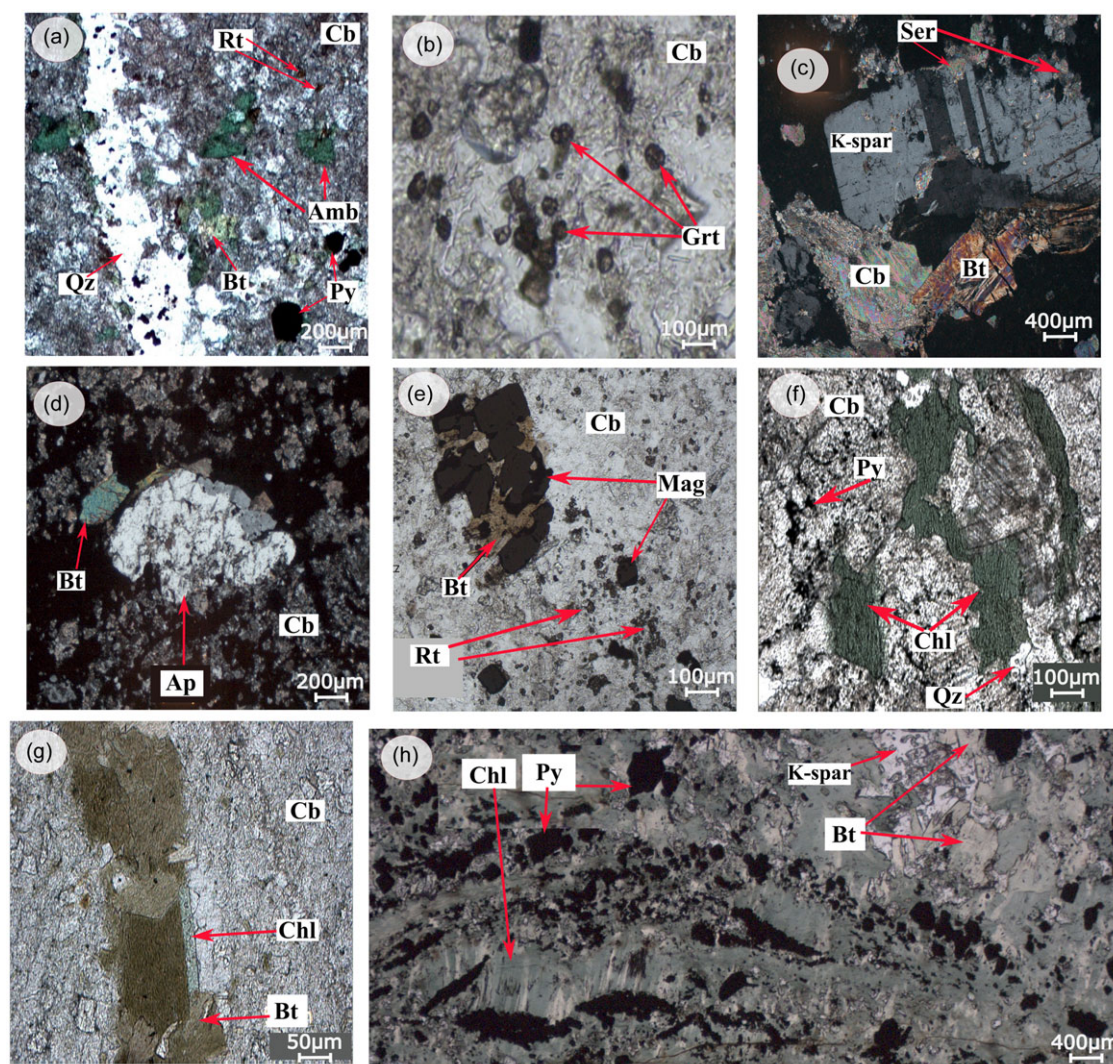


Figure 6. Photomicrographs of minerals present in the alteration zone at Imalia. (a) Pargasite in a carbonate matrix, transected by a quartz vein, with scattered pyrite and rare rutile grains. A few pargasite grains replaced by biotite. (b) Scattered garnet grains in carbonate groundmass. (c) Potassic-rich zone marked by the presence of coarse-grained K-feldspar and biotite. K-feldspar grains are partially replaced by sericite in some areas. (d) Cross-polarised image of rare coarse-grained apatite in close association with biotite and sulphides in a carbonate matrix. (e) Biotite in close proximity to magnetite grains, with scattered rutile in the carbonate groundmass. (f) Coarse-grained Chl1 chlorite in a carbonate groundmass along with quartz and disseminated sulphides. (g) High-resolution image showing a biotite grain partially replaced by chlorite. Chlorite (Chl2) flakes grew at the edge of the biotite crystal, preserving the initial shape of the biotite grain. (h) Chlorite (Chl2) partially altering biotite grains, displaying a typical metasomatic texture in a carbonate groundmass along with quartz, K-feldspar, pyrite, and other sulphides. Abbreviations: Cb – Carbonate, Amb – Amphibole, Bt – Biotite, Qz – Quartz, Ser – Sericite, Py – Pyrite, Grt – Garnet, K-spar – K-feldspar, Ap – Apatite, Rt – Rutile, Mag – Magnetite, Chl – Chlorite.

enriched in Fe and Mn contributed to the formation of ankerite and siderite in the mineralised zone, while ferro-dolomite, another carbonate mineral, is mostly dominant in the distal part of the mineralisation. Calcite is also present in small amounts in the alteration zone.

Iron oxide formation is an important component of the alteration halo at Imalia, mainly consisting of magnetite, along with hematite formed by the replacement of earlier precipitated magnetite. Magnetite is present in the potassic-rich phase, along with biotite and K-feldspar, where it appears subhedral to euhedral with a clean, smooth surface and minor sulphide grains, mainly pyrite, associated with it (Figure 6e). A few magnetite grains are fractured, possibly due to later fluid metasomatism. Rutile, another important oxide, is associated with magnetite in the potassic-rich zone. In the propylitic alteration zone, magnetite is mainly present in disseminated form as subhedral to anhedral grains in close

association with chlorite and epidote (Figure 5b). Magnetite grains in the propylitic alteration zone are highly fractured and, in places, porous, filled with sulphides mainly chalcopyrite and pyrite, and occasionally rare cassiterite (Figures 7d, e). They also display oscillatory zoning in some cases. Ilmenite and titanite are closely associated with magnetite in these samples and are characterised by ilmenite exsolution lamellae in some cases (Figure 7f). Hematite often replaces magnetite in several propylitic samples, though the bulk of the hematite seems to have formed later during the supergene stage. These magnetite-rich samples also hosted rare electrum and indium minerals like roquesite (Tripathi and Deb, 2022).

Sericitization is another hydrothermal alteration product in Imalia (Figure 5e). Sericite is present in small amounts in potassic samples, mostly replacing K-feldspar, likely due to an overprinting episode (Figure 6c). Sericite also has a small presence in the

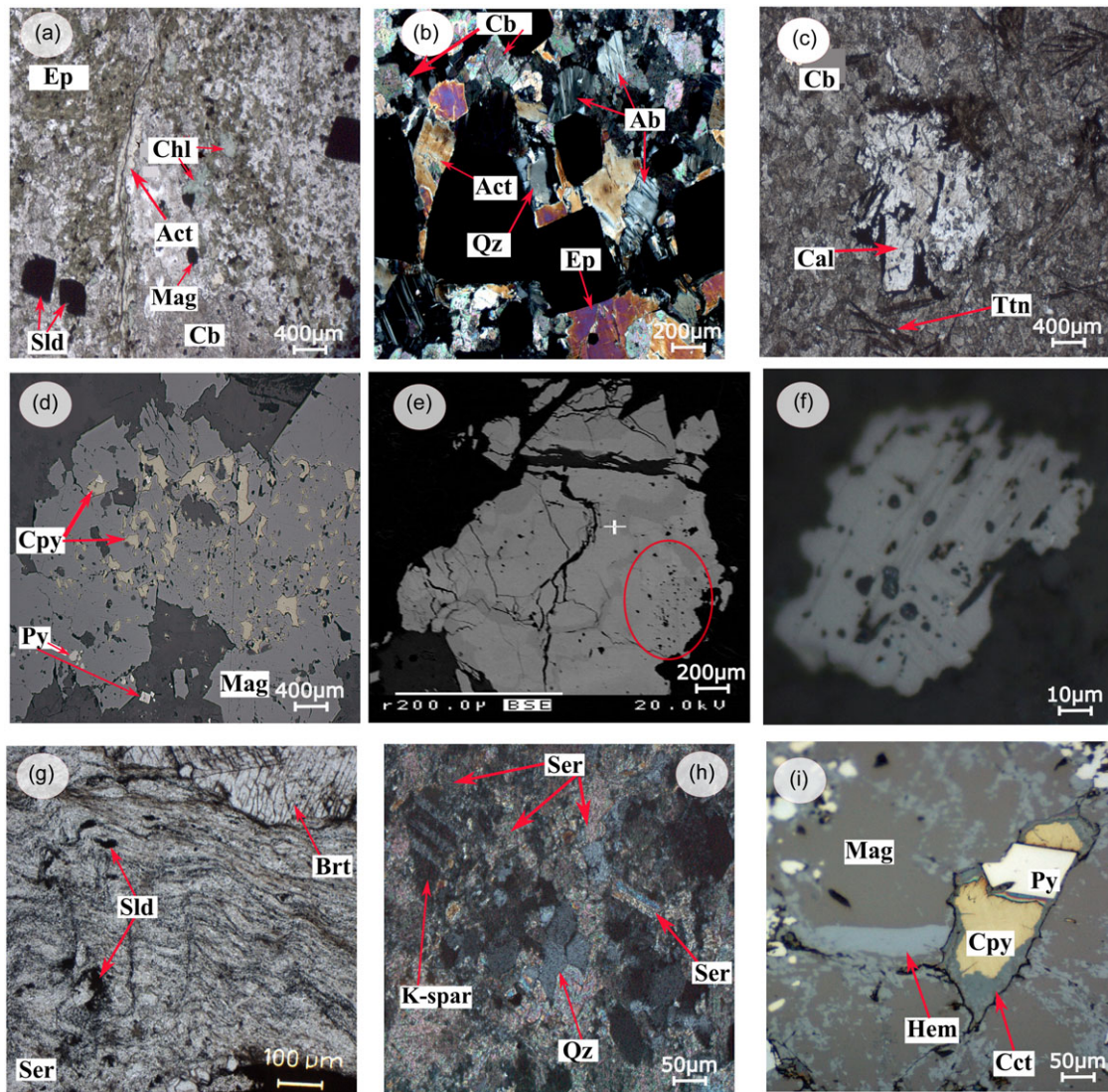


Figure 7. Photomicrographs of minerals present in the alteration zone in Imalia. (a) Co-existing chlorite, epidote, and actinolite in carbonate matrix, along with disseminated ore minerals. (b) Cross-polarised image showing actinolite, albite, epidote, quartz, and carbonate grains in close proximity to coarse ore minerals. (c) Calcite grain with titanite in a recrystallised carbonate groundmass. (d) Reflected light image of a magnetite mass with chalcocopyrite and rare pyrite grains in the chloritised carbonate groundmass. (e) BSE image of highly fractured magnetite grain showing elemental zoning; the area marked with a red circle is a porous domain. (f) Magnetite - ilmenite exsolution lamellae. (g) Sericite-rich sample with disseminated ore minerals and rare barite. (h) Cross-polarised image from the phyllic alteration stage, showing a sericite-rich thin section with quartz. This sericite exhibits a felted texture resulting from the breakdown of feldspar, whose inner margins and twin planes still recognisable. (i) Reflected light image from the supergene stage showing magnetite replaced by hematite, and chalcocopyrite replaced by chalcocite. Abbreviations: Cb - Carbonate, Qz - Quartz, Ser - Sericite, Py - Pyrite, K-spar - K-feldspar, Mag - Magnetite, Ttn - Titanite, Cal - Calcite, Chl - Chlorite, Ab - Albite, Ep - Epidote, Act - Actinolite, Hem - Hematite, Cpy - Chalcocopyrite, Sld - Sulphide, Cct - Chalcocite, Brt - Barite.

chlorite-rich zone as part of the propylitic alteration. However, it becomes more dominant in the later supergene stage. A small amount of quartz, calcite and barite, along with rare witherite and strontianite, are also present in this late stage, representing the zone of hydrolytic alteration in Imalia (Figure 7g). Sericite in many samples pervasively replaces earlier precipitated silicates, often forming a felted texture; faint vestiges of cleavage and twin planes in places indicate the presence of former silicates, although relics of K-feldspar may still be recognisable towards the inner margins of the zone (Figure 7h). Phyllic alteration gradually grades into argillic alteration in Imalia but is not widespread, evident mainly as localised kaolinization observed mostly in surface samples and a few subsurface borehole samples. This occurred during the supergene stage, where kaolinite formed along with goethite,

hematite, sericite and quartz, primarily overprinting the earlier alteration and closely related to the increasing influence of meteoric fluids. The localised kaolin formations on the surface appear to be due to weathering effects. The supergene stage in Imalia is associated with chalcocite and covellite formation through replacement of earlier precipitated chalcocopyrite. In many samples from the supergene stage, magnetite grains are martitised, resulting in the formation of hematite (Figure 7i). Limonitization has been observed in borehole samples close to the surface, where rare malachite encrustations can also be seen.

Pervasive silicification of the carbonate lithology is widespread in the mineralised zone. Quartz is ubiquitously present in samples, from potassic to argillic alteration. On the surface and in the subsurface (borehole samples), the expression of hydrothermal

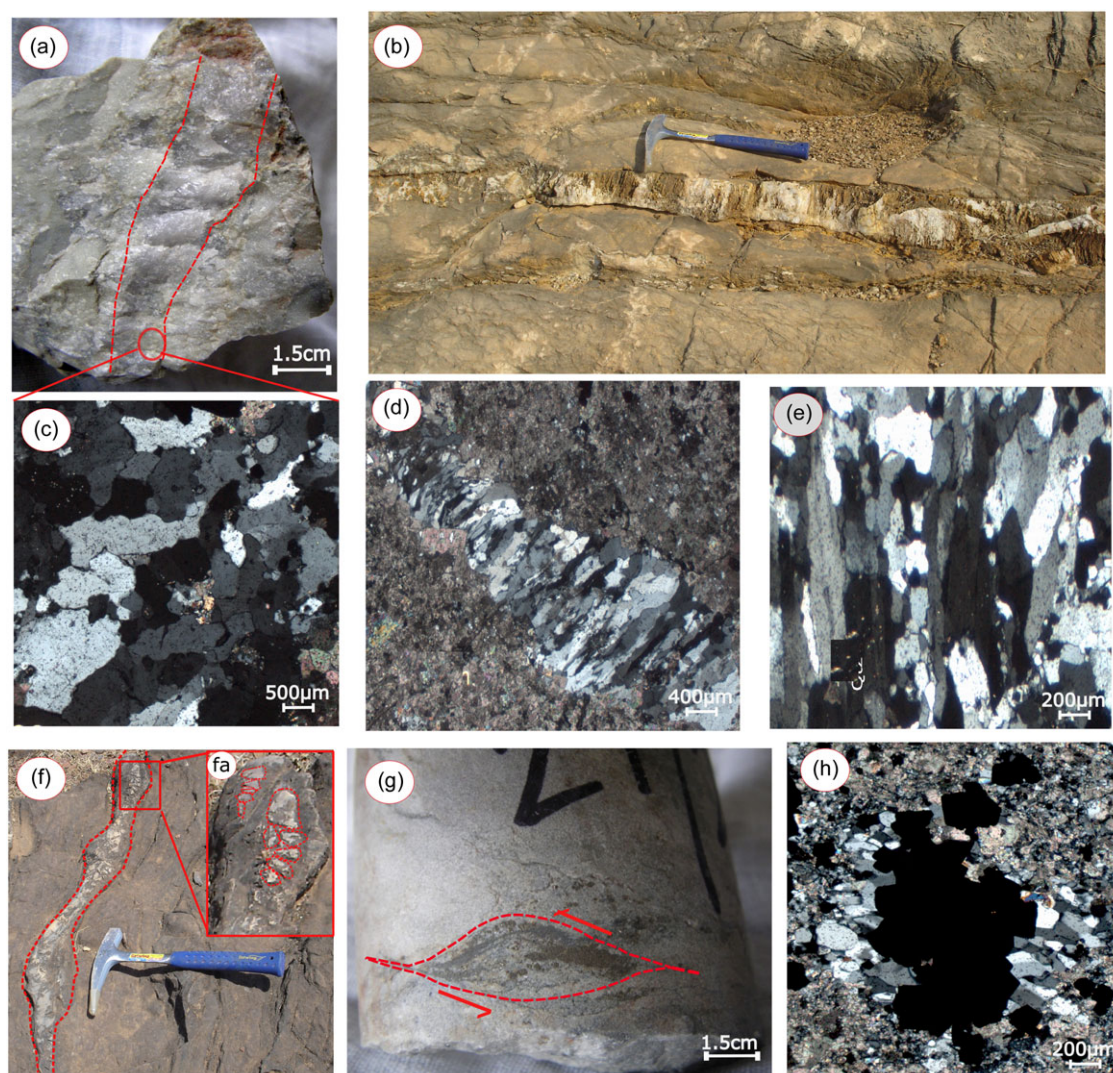


Figure 8. Mesoscopic and microscopic images showing the nature of silicification in Imalia. (a) Barren buck quartz vein in recrystallised dolostone. (b) Fibrous quartz vein in recrystallised dolostone. (c), (d), (e) Microscopic images of buck, fibrous, and comb quartz veins, respectively. (f) Quartz boudinage forming dilation breccia. (fa) Enlarged view showing dilation breccia. (g) Sigmoidal quartz vein filled with sulphides, showing evidence of shearing. (h) Quartz pressure fringes around sulphide mineral.

alteration is seen in the form of jasperoidal masses. Most jasperoids are conformable to the shear zone, and some sub-surface samples appear to have formed by completely replacing host carbonate, with rare associated sulphides and occasional limonitic disseminations (Figure 5f). Silicification during the hydrothermal surge is also manifested as thin quartz veins in the carbonate lithology. On the surface, the quartz veins range in width from less than a metre to as much as 2 metres and are traceable up to 15 metres in length. In borehole samples, silicification is represented by silicified dolostone and a diverse set of quartz veins, ranging from barren to mineralised. Most quartz veins have a translucent milky base with numerous small fluid inclusions, making fluid inclusion studies difficult. The barren quartz veins display a buck texture and are characterised by euhedral to anhedral grains of variable size tightly stacked throughout the vein (Figures 8a, c). Quartz veins in Imalia often show fibrous and comb textures. In thin sections, fibres are optically continuous and often show undulose extinction. Crystals may taper slightly at the base, corresponding to crystallisation coeval with vein opening (Figures 8b, d). Some thin sections show quartz veins, mostly tapered at their bases, giving a comb-shaped

appearance (Figure 8e). The comb texture is occasionally filled with sulphides. In the mineralised zone, quartz boudins and sigmoidal veins were also identified (Figures 8f, g), with some filled with sulphides. Another common form of silica deluge in the mineralised zone is the presence of sharp-edged quartz pressure fringes close to ore minerals (Figure 8h). Extensive brecciation due to hydrothermal activity has been observed in both surface and borehole samples from the mineralised zone. Some breccia samples show rupturing of the host dolostone or earlier-formed quartz veins with little or no displacement, indicative of crackle breccia formation (Figure 9a). From the propylitic alteration zone, dolostone samples of tectonic breccia with a monogenic nature, grain reduction, oriented fragments, and matrix-supported features were observed (Figure 9b). Some similar-appearing breccias in the mineralised zone were filled with sulphides (Figure 9c). Collapse breccia was also identified in Imalia, characterised by a large variation in fragment size, sharp-angled comb fragments and grain-supported nature (Figure 9d), formed as a result of increased spalling of vein walls during hydrothermal fluid movement. In a few brittle quartz vein boudins dilational

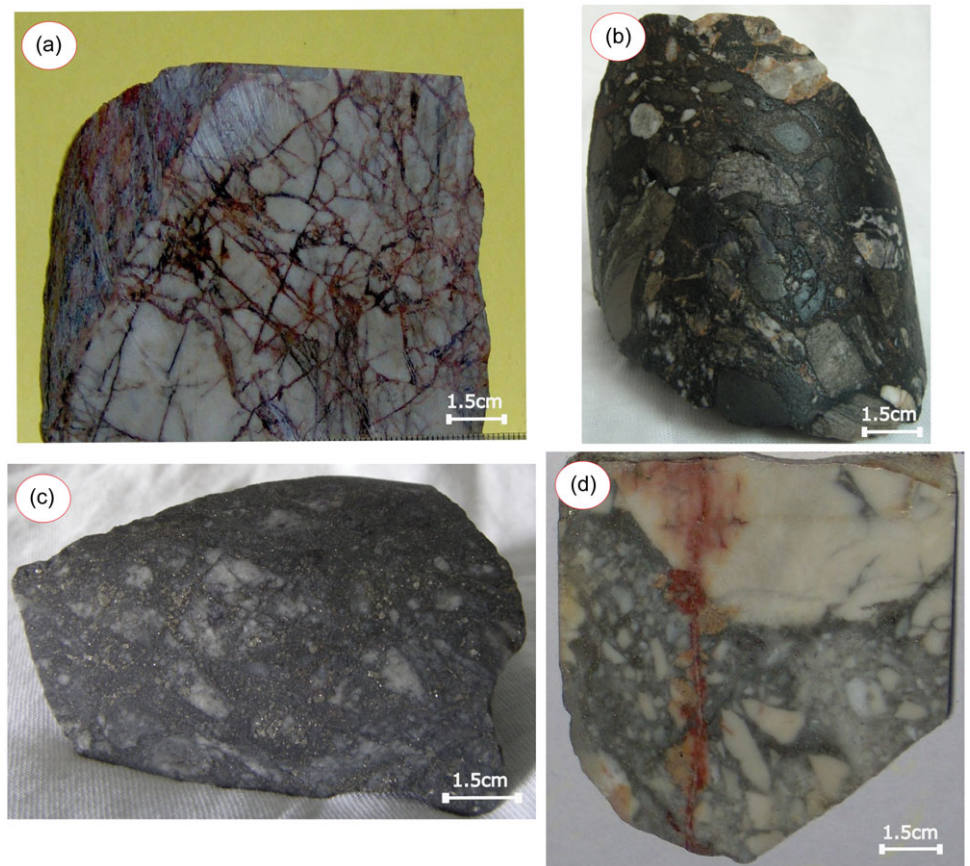


Figure 9. Images showing different types of breccia present in the Imalia deposit, based on the classification of breccia by Jébrak (1997), and Chauvet (2019). (a) A sample of crackle breccia formed at the onset of hydrothermal activity. (b) A sample of tectonic breccia characterised by grain reduction, monogenic nature, and fragments with preferred orientation. (c) Hand specimen of tectonic breccia from the mineralised zone, with disseminated sulphides. (d) A sample of collapse breccia characterised by variation in fragments size and often having combed fragments.

breccia signatures were observed, formed during shearing to create space for the movement of hydrothermal fluid (Figure 8fa).

The paragenetic table (Figure 10), based on petrographic study, denotes the sequence and overlap of the formation of this diverse range of silicates and oxides in the alteration halo associated with type 3 and type 4 mineralisation. It also includes the order of precipitation of the whole range of sulphides, including rare phases associated with vein-type mineralisation. In brief, apart from oxide minerals like magnetite, ilmenite, titanite, rutile and rare cassiterite, a small amount of sulphides, including chalcopyrite, pyrite, rare electrum and indium mineral roquesite were present in type 3 ore samples. In type 4 ore samples, a large array of sulphides and oxides including pyrite, arsenopyrite, fahlore, chalcopyrite, electrum and cassiterite, along with a number of rare phases like aikinine, idaite, enargite and ourayite, were identified (cf. Tripathi and Deb, 2022).

Due to the small size of fluid inclusions in the associated carbonate/quartz grains, limited data were obtained from type 3 (alteration zone) and type 4 ore samples (Tripathi, 2008). However, the results still provided valuable insights into the behaviour of the hydrothermal fluid during the alteration stage and subsequent sulphide mineralisation, which are summarised below. Petrographic study of wafers indicated the presence of three types of fluid inclusions at room temperature: primary aqueous bi-phase inclusions (V+L), (L+V) inclusions, and three-phase aqueous liquid + liquid CO₂ + vapour CO₂ inclusions. Aqueous inclusions constitute around 90% of the total studied inclusions, while carbonic-rich inclusions are present in smaller proportions. The

fluid inclusion data show that the hydrothermal fluid initially had higher temperatures and salinities in type 3 ore wafers, ranging from 280°C to 509°C and salinities from 6 to 23 wt% NaCl, rich in both carbonic and aqueous fluid inclusions. Wafers from type 4 ore samples display homogenisation temperatures between 125°C and 290°C, with salinities ranging from 3.2 to 11.7 wt% NaCl, dominated mostly by aqueous fluid inclusions. The coexisting aqueous and carbonic fluid inclusions in type 3 ore wafers suggest a possible boiling event during the initial stages of hydrothermal activity at Imalia (Bodnar *et al.* 1985; Goldstein and Reynolds, 1994; Tripathi, 2008). In brief, the results indicate that the hydrothermal fluid initially generating the alteration halo was rich in carbonic inclusions with moderate salinities and higher homogenisation temperatures. Later, fluid immiscibility during CO₂ gas escape led to increased salinities in fluid inclusions. Subsequently, the hydrothermal fluid began mixing with meteoric water as it moved to shallower levels, resulting in a decrease in homogenisation temperature and salinities during the main sulphide precipitation stage.

4.b. Mineral chemistry of hydrothermal minerals

All silicate, carbonate and oxide minerals identified in the petrographic study from the alteration zone underwent electron probe micro-analyses to understand their compositional characteristics. A summary of the compositional data in the form of maximum and minimum concentration of all analysed silicates and oxides minerals of the alteration zone is provided in Table 1,

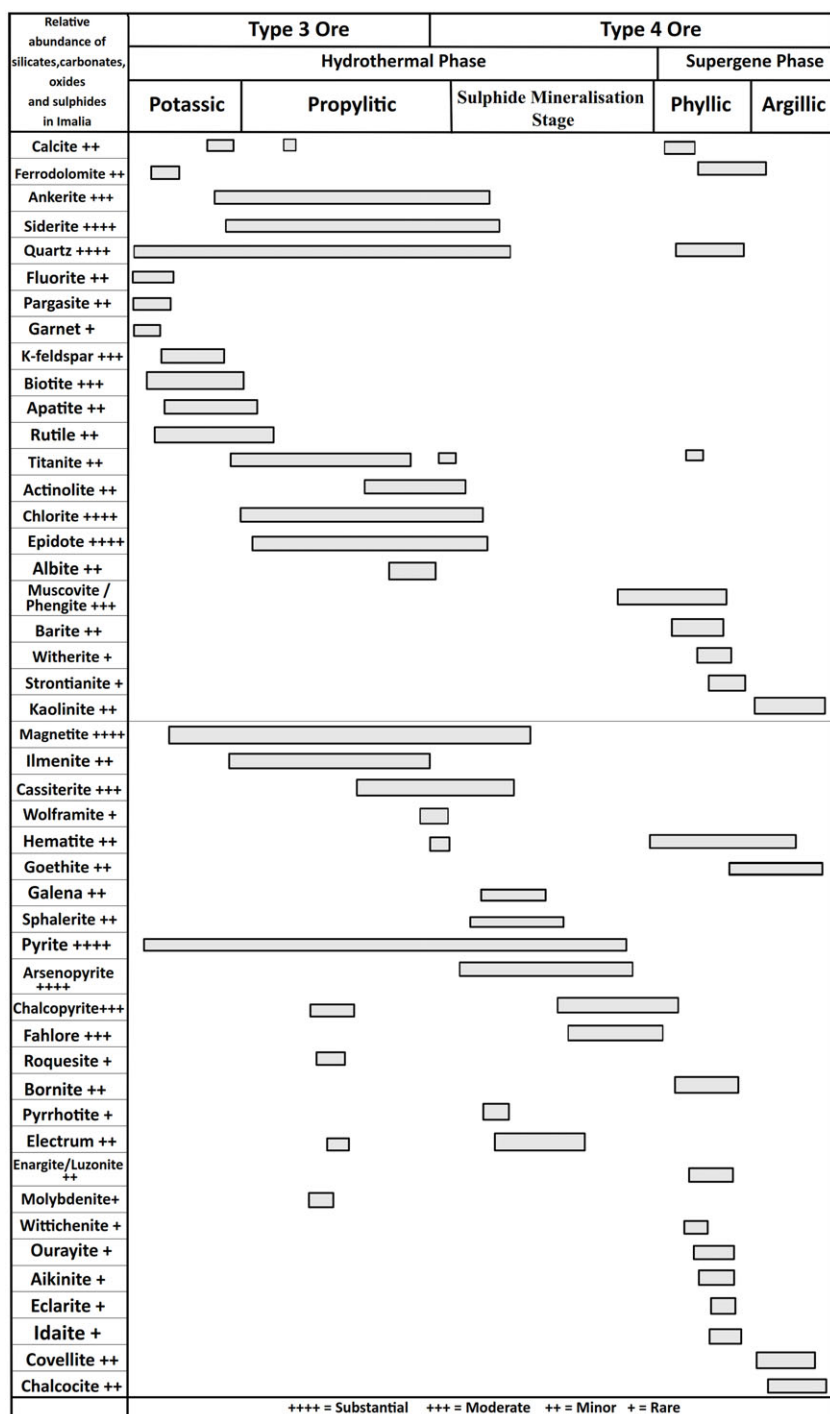
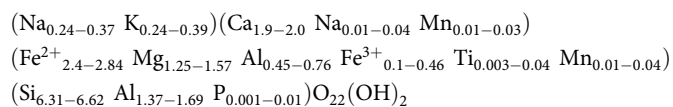


Figure 10. The paragenetic sequence of minerals in hydrothermal alteration and mineralisation associated with type 3 and type 4 ore, and their relative abundance in the Imalia deposit.

with complete compositional data in appendix (Supplementary Table S1).

Hydrothermal amphiboles from Imalia, based on their mineral composition, can be classified as Ca-amphiboles according to the classification scheme of Hawthorne *et al.* (2012), with Ca concentrations ranging from 1.9 to 2 per formula unit (pfu). These Ca-amphiboles can be further subdivided into two groups. The first group, formed during the initial stage of hydrothermal activity, can be categorised as pargasite (Figure 11a). These amphiboles are relatively homogeneous with minimal compositional variation (details are in Supplementary Table S1). The mineral formula for pargasite amphiboles from Imalia,

calculated using the spreadsheet program by Hawthorne *et al.* (2012) based on 23 oxygen atoms, is:



The second group of Ca-amphiboles, which formed later along with propylitic minerals, falls into the actinolite mineral group (Figure 11b). The actinolite grains show minor elemental variations in their major elements (see Supplementary Table

Table 1. Statistical data (maximum, minimum, mean values, and number of analyses) of electron probe microanalysis of silicates, carbonates and oxides present in the Imalia deposit

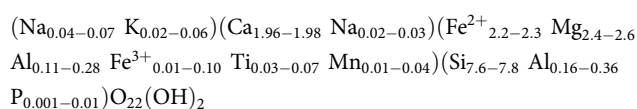
| Mineral | Analysis Number | | wt% | wt% | wt% | wt% | wt% | wt% | wt% | wt% | wt% | | |
|-------------------|--------------------------|--------|------------------|------------------|--------------------------------|------|------|------|------|-------------------|------------------|------|------|
| | | | SiO ₂ | TiO ₂ | Al ₂ O ₃ | MnO | FeO | MgO | CaO | Na ₂ O | K ₂ O | BaO | |
| Pargasite | N - 10 | Max | 43.3 | 0.4 | 13.0 | 0.3 | 23.1 | 6.9 | 12.2 | 1.2 | 2.0 | | |
| | | Min | 40.4 | 0.2 | 10.1 | 0.03 | 22.3 | 5.4 | 11.6 | 0.9 | 1.2 | | |
| | | Mean | 41.5 | 0.3 | 12.2 | 0.3 | 22.7 | 5.9 | 11.8 | 1.2 | 1.6 | | |
| Actinolite | N - 8 | Max | 52.9 | 0.06 | 3.4 | 0.3 | 18.7 | 11.7 | 12.5 | 0.3 | 0.3 | | |
| | | Min | 51.2 | 0.03 | 1.9 | 0.2 | 17.9 | 10.7 | 12.3 | 0.2 | 0.1 | | |
| | | Mean | 52.1 | 0.05 | 2.5 | 0.2 | 18.2 | 11.2 | 12.4 | 0.3 | 0.2 | | |
| Garnet | N - 6 | Max | 36.9 | 0.05 | 20.7 | 4.0 | 35.8 | 1.4 | 5.1 | | | | |
| | | Min | 36.2 | 0.05 | 20.4 | 2.9 | 32.9 | 1.1 | 1.5 | | | | |
| | | Mean | 36.6 | 0.05 | 20.5 | 3.4 | 34.5 | 1.2 | 3.5 | | | | |
| Epidote | N - 12 | Max | 40.5 | 0.1 | 27.0 | 0.2 | 12.3 | 0.2 | 24.3 | 0.08 | 1.3 | | |
| | | Min | 38.1 | 0.01 | 23.6 | 0.01 | 5.4 | 0.01 | 22.1 | 0.02 | 0.01 | | |
| | | Mean | 38.7 | 0.05 | 25.3 | 0.09 | 9.8 | 0.05 | 23.4 | 0.05 | 0.2 | | |
| Feldspar | K-feldspar | N - 11 | Max | 65.1 | 0.05 | 18.6 | | 0.2 | 0.02 | 2.7 | 0.8 | 16.9 | 0.3 |
| | | | Min | 62.3 | 0.05 | 17.7 | | 0.01 | 0.01 | 0.02 | 0.3 | 16.1 | 0.01 |
| | | | Mean | 64.3 | 0.05 | 18.3 | | 0.1 | 0.01 | 0.3 | 0.4 | 16.3 | 0.1 |
| | Plagioclase | N - 15 | Max | 73.1 | 0.1 | 23.5 | 0.07 | 0.3 | 0.05 | 5.1 | 11.7 | 0.1 | 0.05 |
| | | | Min | 61.7 | 0.01 | 16.4 | 0.01 | 0.01 | 0.01 | 0.12 | 8.7 | 0.01 | 0.01 |
| | | | Mean | 66.5 | 0.05 | 20.8 | 0.04 | 0.06 | 0.02 | 2.3 | 9.9 | 0.06 | 0.02 |
| Mica | N - 15 | Max | 51.5 | 0.5 | 36.3 | 0.08 | 5.0 | 4.4 | 1.0 | 1.2 | 10.4 | 0.2 | |
| | | Min | 45.8 | 0.1 | 24.3 | 0.01 | 0.6 | 0.4 | 0.3 | 0.1 | 8.8 | 0.01 | |
| | | Mean | 47.9 | 0.2 | 31.6 | 0.03 | 2.3 | 1.9 | 0.6 | 0.6 | 9.5 | 0.1 | |
| Carbonate | Calcite | N - 7 | Max | 0.2 | 0.1 | 0.3 | 1.5 | 1.2 | 0.9 | 54.4 | | | |
| | | | Min | 0.03 | 0.01 | 0.06 | 0.2 | 0.7 | 0.5 | 54.1 | | | |
| | | | Mean | 0.1 | 0.03 | 0.2 | 0.9 | 0.9 | 0.6 | 54.2 | | | |
| | Siderite | N - 7 | Max | 0.3 | 0.05 | 0.1 | 17.8 | 42.7 | 9.1 | 1.0 | 0.04 | 0.03 | |
| | | | Min | 0.07 | 0.03 | 0.03 | 5.2 | 32.6 | 4.3 | 0.6 | 0.01 | 0.03 | |
| | | | Mean | 0.2 | 0.04 | 0.08 | 12.3 | 38.3 | 6.3 | 0.8 | 0.02 | 0.03 | |
| | Dolomite-Ankerite series | N - 7 | Max | 3.0 | 0.06 | 0.02 | 8.5 | 13.5 | 12.6 | 27.1 | 0.04 | 0.03 | |
| | | | Min | 0.01 | 0.06 | 0.02 | 4.7 | 11.5 | 7.9 | 25.9 | 0.02 | 0.03 | |
| | | | Mean | 1.0 | 0.06 | 0.02 | 7.6 | 12.1 | 9.1 | 26.3 | 0.03 | 0.03 | |
| Biotite | N - 21 | Max | 39.3 | 2.0 | 18.3 | 0.3 | 22.6 | 16.7 | 0.6 | 0.07 | 10.1 | 0.1 | |
| | | Min | 34.3 | 0.2 | 13.2 | 0.01 | 13.2 | 7.1 | 0.01 | 0.02 | 6.6 | 0.03 | |
| | | Mean | 38.1 | 1.1 | 14.6 | 0.1 | 16.9 | 14.0 | 0.1 | 0.05 | 8.9 | 0.06 | |
| Chlorite | Chl1 | N - 21 | Max | 26.2 | 0.3 | 20.9 | 0.7 | 27.4 | 15.5 | 0.2 | 0.08 | 0.05 | |
| | | | Min | 24.8 | 0.01 | 18.9 | 0.2 | 25.8 | 13.2 | 0.01 | 0.01 | 0.01 | |
| | | | Mean | 25.6 | 0.1 | 19.6 | 0.4 | 26.5 | 14.2 | 0.07 | 0.03 | 0.03 | |
| | Chl2 | N - 15 | Max | 28.0 | | 18.5 | 0.5 | 26.3 | 18.2 | 0.6 | | 0.1 | |
| | | | Min | 26.8 | | 17.8 | 0.04 | 22.7 | 15.4 | 0.01 | | 0.02 | |
| | | | Mean | 27.6 | | 18.1 | 0.3 | 24.4 | 16.8 | 0.1 | | 0.04 | |
| Rutile | N - 5 | Max | 0.06 | 99.3 | 0.02 | | 0.1 | 0.01 | 0.05 | | 1.3 | | |
| | | Min | 0.01 | 98.8 | 0.01 | | 0.07 | | 0.01 | | 0.5 | | |
| | | Mean | 0.04 | 99.1 | 0.01 | | 0.1 | | 0.02 | | 1.0 | | |

(Continued)

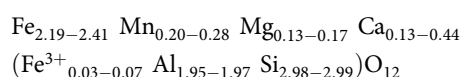
Table 1. (Continued)

| Mineral | Analysis Number | | wt% | wt% | wt% | wt% | wt% | wt% | wt% | wt% | wt% | |
|-----------|-----------------|------|------------------|------------------|--------------------------------|------|------|------|------|-------------------|------------------|------|
| | | | SiO ₂ | TiO ₂ | Al ₂ O ₃ | MnO | FeO | MgO | CaO | Na ₂ O | K ₂ O | BaO |
| Titanite | N - 6 | Max | 30.7 | 37.7 | 2.2 | 0.1 | 0.9 | | 28.9 | | 0.1 | 0.7 |
| | | Min | 30.2 | 36.2 | 1.5 | 0.01 | 0.9 | | 28.4 | | 0.01 | 0.01 |
| | | Mean | 30.5 | 36.9 | 1.8 | 0.1 | 0.9 | | 28.7 | | 0.04 | 0.4 |
| Magnetite | N - 17 | Max | 0.2 | 0.09 | 0.04 | 0.3 | 94.9 | 0.05 | | | | |
| | | Min | 0.01 | 0.01 | 0.01 | 0.04 | 89.1 | 0.01 | | | | |
| | | Mean | 0.1 | 0.05 | 0.02 | 0.1 | 93.0 | 0.03 | | | | |
| Ilmenite | N - 11 | Max | 0.09 | 55.5 | 0.03 | 5.0 | 44.3 | 0.1 | | | | 0.8 |
| | | Min | 0.07 | 51.2 | 0.01 | 2.2 | 38.9 | 0.01 | | | | 0.2 |
| | | Mean | 0.08 | 53 | 0.02 | 3.7 | 42.5 | 0.08 | | | | 0.5 |

S1). The mineral formula for actinolites from Imalia, based on 23 oxygen atoms, is:

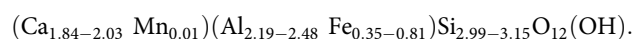


The EPMA data for the small amount of garnet present in Imalia showed minor compositional variation. The average concentration of the main components in these garnets is 36.6 wt% SiO₂, 20.5 wt% Al₂O₃ and 34.5 wt% FeO, with small amounts of MnO, MgO and CaO. The mineral formula for garnet from Imalia, based on 12 oxygen atoms pfu, is:



The data indicate that the garnets from the Imalia deposit generally form an almandine-pyrope-grossular solid solution. They are Fe-Al-rich, dominated by almandine (73.5–80.9 mol%), with less grossular (4.3–14.5 mol%), along with minor amounts of spessartine (6.7–9.3 mol%), pyrope (4.5–5.9 mol%) and andradite (0.2–0.4 mol%) (Figure 11c).

Next to chlorite, epidote is one of the most abundant propylitic minerals found in the alteration zone. The electron microprobe data for epidote did not show significant variation in the concentration of main elements (see Supplementary Table S1). Overall, the epidotes are alumina-rich, with some variation in Fe composition. Al and Fe exhibit an excellent negative correlation across all analysed samples, with an R value of -0.9, suggesting a complete solid solution between them. Additionally, Fe does not show a linear correlation with Ca, having an R value of 0.01. These relationships are consistent with Fe being present entirely as Fe³⁺, or if present as Fe²⁺, substituting for Al in the octahedral M sites. Thus, the calculations assume all Fe as Fe³⁺, based on 12.5 oxygen equivalents. In the Fe³⁺ and Al³⁺ plot, most analysed grains fall into the epidote field, with some in the clinzoisite field (Figure 11d). An average formula for epidote solid solution from Imalia is:



Epidote composition is also expressed in terms of mole fraction of the component Ca₂Fe₃Si₃O₁₂(OH) (Pistacite) in the clinzoisite-epidote series. In Imalia, pistacite values (Ps) for epidote range from 12 to 27.

Feldspars are an important silicate phase present both in the alteration zone and in the non-mineralised dolostone with phyllic intercalations. K-feldspar is found in close association with biotite in the potassic phase. These K-feldspars have an average concentration of 1.0 pfu Al and 0.97 pfu K. In the ternary feldspar plot, they lie in the orthoclase field. The calculated formula for K-feldspar from Imalia, based on 23 oxygen atoms, is: (K_{0.95-1.0} Na_{0.03-0.07}) (Al_{1.0-1.02} Fe_{0.01}) (Si_{2.9-3.0}) O₈. Microanalyses show that the hydrothermal K-feldspar has a composition ranging from Or 84.9 to Or 97.3 (Figure 12a). In the propylitic zone, plagioclase is found in close association with chlorite, epidote and actinolite. The plagioclase grains in the mineralised dolostone have an average Na content of 0.84 cations pfu. There is significant variation in Ca composition, ranging from 0.01 to 0.25 pfu, while Al has a mean concentration of 1.08, with Fe and Mn in insignificant concentrations. In the ternary feldspar plot, the analysed plagioclase lies in the albite and oligoclase fields (Figure 12a). The calculated formula for plagioclase from Imalia, based on 23 oxygen atoms, is: (Na_{0.75-1.0} Ca_{0.01-0.25}) (Al_{0.84-1.2} Si_{2.76-3.17}) O₈. Microprobe analyses show the composition of plagioclase ranging from Ab 75.43 to Ab 99.6.

Sericite, in the form of muscovite and phengite, are the two important micaceous minerals present in the alteration zone. The Si concentration of the analysed muscovite grains in Imalia, based on 11 oxygen atoms, range from 3.08 to 3.14 pfu, while the phengite concentration range from 3.42 to 3.46 pfu. The distribution of these mica categories can be observed by plotting the total Al cations pfu against the summed total of the Si + Mg + Fe cations (Figure 12b). The data define a linear array presumably reflecting Tschermak substitution (i.e., silicon, iron and magnesium substituting for aluminium). Muscovite, with a chemical formula of [K(Al₂) AlSi₃O₁₀(OH)₂]₂, has a substitution index of 1. Values >1 indicate an increased celadonite component. Muscovite in the Imalia deposit has an average substitution index of 1.17, while phengite has an average substitution index of 2.12.

Since carbonate rocks are the host lithology in Imalia, the interaction of hydrothermal fluid can be traced in the mineral

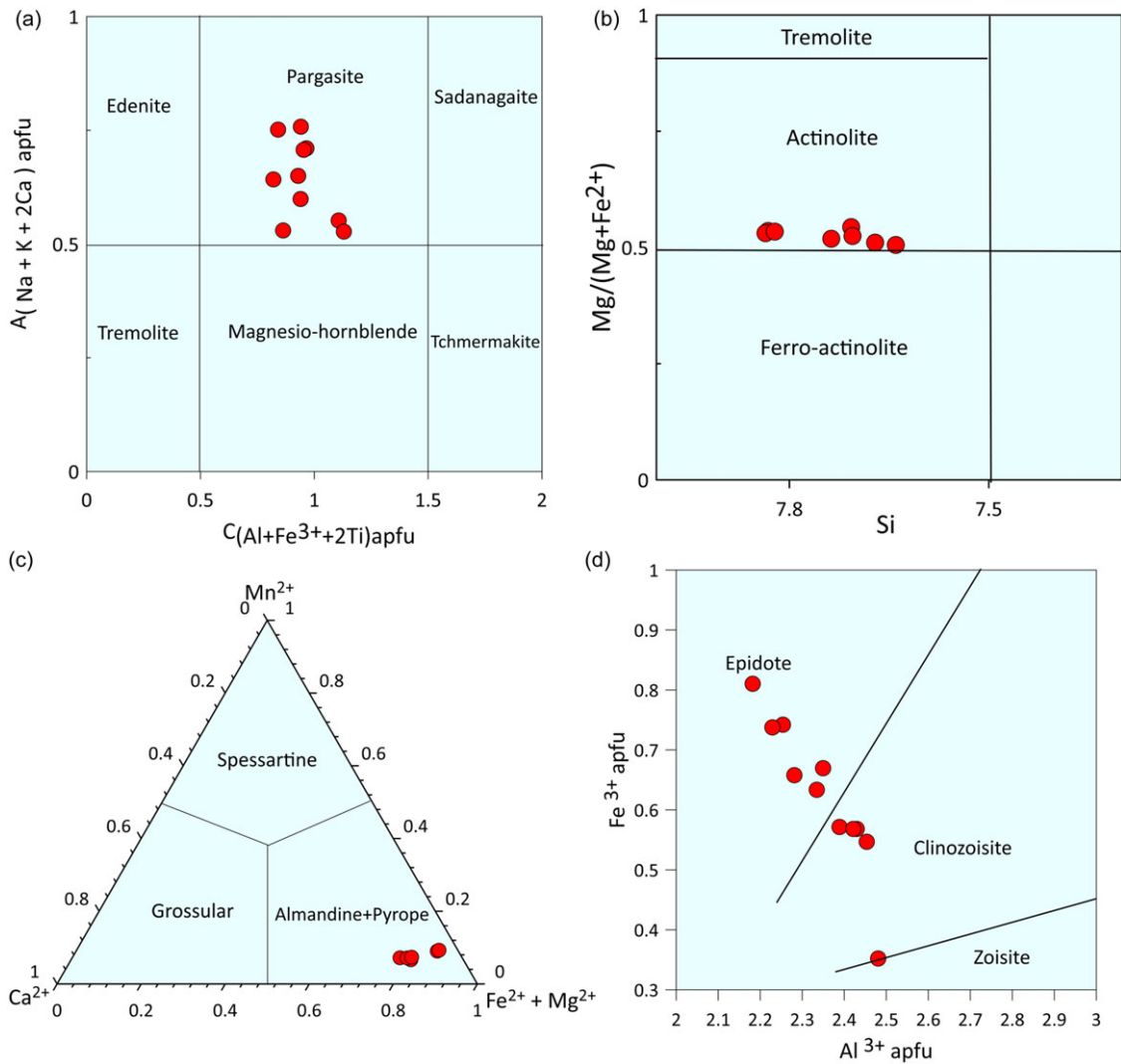


Figure 11. Diagrams showing the compositional variations of different minerals present in the alteration zone at Imalia. (a) Amphibole classification diagram (after Hawthorne *et al.* 2012). Pargasite is the dominating calcic-amphibole species in the analysed grains, with $\text{Si} < 7.25$ and $(\text{Na} + \text{K})_{\text{A}} > 0.5$. (b) Amphibole classification diagram showing amphiboles with compositions $\text{Si} > 7.25$ and $(\text{Na} + \text{K})_{\text{A}} < 0.5$, belonging to tremolite-actinolite series. (after Leake *et al.* 1997). (c) Ternary diagram showing the composition of garnet from the alteration zone. (d) Classification of minerals in the epidote group on a Fe^{3+} vs Al^{3+} diagram, based on Franz and Liebscher (2004).

chemistry of the carbonates. The electron probe data for the carbonates can be grouped into three categories. The first category is calcite, which is present in small amounts in the alteration zone. The calcite grains have an average concentration of 95.7 mol% CaCO_3 , 1.7 mol% MgCO_3 , 1.3 mol% FeCO_3 and 1.9 mol% MnCO_3 , indicating a non-stoichiometric nature. The other two categories include minerals formed by an incremental increase in Fe and Mn concentrations in the host dolostone. These belong to the dolomite-ankerite solid solution series and the siderite-rhodochrosite-magnesite solid solution series. Carbonates of the dolomite-ankerite series have an average concentration of 48.4 mol% CaCO_3 , 23.4 mol% MgCO_3 , 17.4 mol% FeCO_3 and 10.8 mol% MnCO_3 , while those of the siderite-rhodochrosite-magnesite series have an average concentration of 1.6 mol% CaCO_3 , 17.0 mol% MgCO_3 , 60.8 mol% FeCO_3 and 20.6 mol% MnCO_3 . Ferro-dolomite mineral is mostly found in the distal part of the alteration zone, while carbonates in the proximal part of the mineralisation are predominantly ankerite and siderite. The

triangular plot showing the distribution of carbonates in the alteration zone is shown in Figure 12c.

The EPMA results for biotite are summarised in Table 1. The formula for biotite is based on 22 oxygen atoms, and the average formula for biotite from the alteration zone, using the Mica+ program (Yuvaz, 2003), is: $\text{K}_{0.64-0.97} \text{Mg}_{1.62-1.87} \text{Fe}_{0.84-1.15} \text{Al}_{1.19-1.31} \text{Si}_{2.83-3.0} \text{Ti}_{0.01-0.1} \text{Mn}_{0.01-0.02} \text{O}_{22}(\text{OH})_4$. The biotite grains do not show significant substitution at the interlayer position. The main substitution is Fe, with minor contributions from Al^{VI} , Ti and Mn. Fe, Ti and Al^{VI} account for up to one-third of the occupancy of the octahedral sites. The sum of the octahedral cations of biotite from the alteration zone in most analyses is less than the ideal value of 3 cations pfu. This discrepancy is largely due to trioctahedral-dioctahedral solid solution through cation substitutions of the type $[2\text{R}^{3+} + \square = 3\text{R}^{2+} (\square \text{vacancy})]$ (Foster, 1960). The biotite composition, when plotted on a ternary compositional variation diagram based on Foster (1960), falls into the Mg-biotite field (Figure 12d). Beane

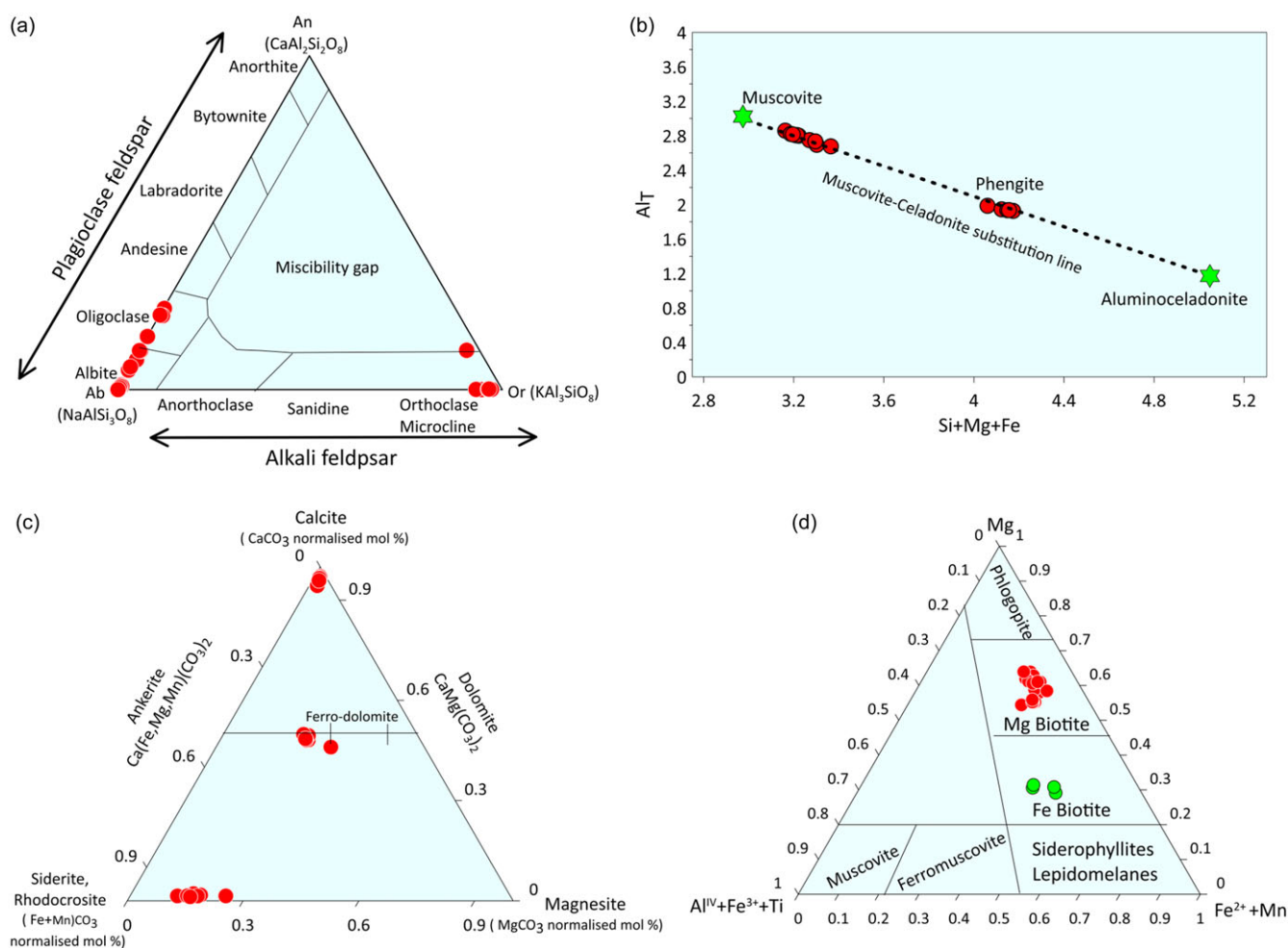


Figure 12. Diagrams showing the compositional variations of different minerals present in the alteration zone at Imalia. (a) Ternary composition diagram for minerals of the feldspar group, based on the diagram of Deer *et al.* (1992). (b) A plot of Al_I (pfu) versus sum of Si, Mg and Fe (pfu) for the phengites. The dashed line indicates the theoretical heterovalent substitution of $Al^{VI}Al^{IV} \leftrightarrow (Mg,Fe)^{VI}Si^{IV}$ for charge-balancing in the phengite-series solid solution. (c) Ternary plot showing composition of carbonates. (d) Chemical composition of biotite on the classification diagram (after Foster, 1960). Red circles represent samples of biotite from alteration zone, while green circles represent biotite from phyllitic intercalated dolostone.

(1974) found that magmatic biotites generally have molecular ratios of $Mg/Fe < 1.0$, whereas hydrothermal biotites are characterised by $Mg/Fe > 1.5$ and $Fe^{3+}/Fe^{2+} < 0.3$. The hydrothermal biotite from the alteration zone at Imalia has an average Mg/Fe ratio of 1.83 and average Fe^{3+}/Fe^{2+} values of 0.17, indicating its hydrothermal nature. Biotite is also present in minor amounts in the host dolostone with phyllitic intercalations, which have been partially replaced by chlorite during propylitic alteration. EPMA analyses of these biotites showed they were rich in Al and Fe and poor in Mg (see Supplementary Table S1). When plotted on the ternary diagram of Foster (1960), they lie in the Fe-biotite field (Figure 12d).

Since chlorite is the most dominant silicate present in the Imalia alteration zone, its mineral chemistry is crucial to understanding the conditions during its formation. EPMA results for chlorite are listed in Supplementary Table S1. The formula for chlorite, based on 14 oxygen atoms pfu, is: (Chl-1) $Mg_{2.16-2.48} Al_{2.42-2.59} Fe_{2.32-2.46} Mn_{0.02-0.06} Si_{2.70-2.80} O_{10}(OH)_8$, and for (Chl-2)

$Mg_{2.42-2.82} Al_{2.20-2.34} Fe_{1.98-2.32} Mn_{0.003-0.04} Si_{2.86-2.93} O_{10}(OH)_8$. According to Hillier and Velde (1991), the presence of illite and/or smectite intergrown with chlorite often results in elevated $(Na_2O + K_2O + CaO)$ contents in chlorite. To assess such potential contamination of chlorite chemistry, a benchmark of $wt. (Na_2O + K_2O + CaO) < 0.5\%$ is proposed (with values $> 0.5\%$ suggesting contamination). All EPMA dataset used in this study adhere to the criterion of $(Na_2O + K_2O + CaO) wt. < 0.5\%$, indicating negligible contamination of Imalia chlorite chemistry and confirming its suitability for further analysis. The classification by Zane and Weiss (1998), based on $(Al + \square) - Mg - Fe$, is used to classify chlorite. In Figure 13a, both Chl-1 and Chl-2 chlorites are trioctahedral, characterised by full tetrahedral occupancy and nearly full octahedral occupancy. The number of vacant octahedral sites (\square) per six positions is < 0.2 . Both Chl-1 and Chl-2 lean towards the clinocllore field. According to Wiewióra and Weiss (1990), both chlorites plot close to the amesite - Al-free chlorite line, which is parallel to the Tschermak

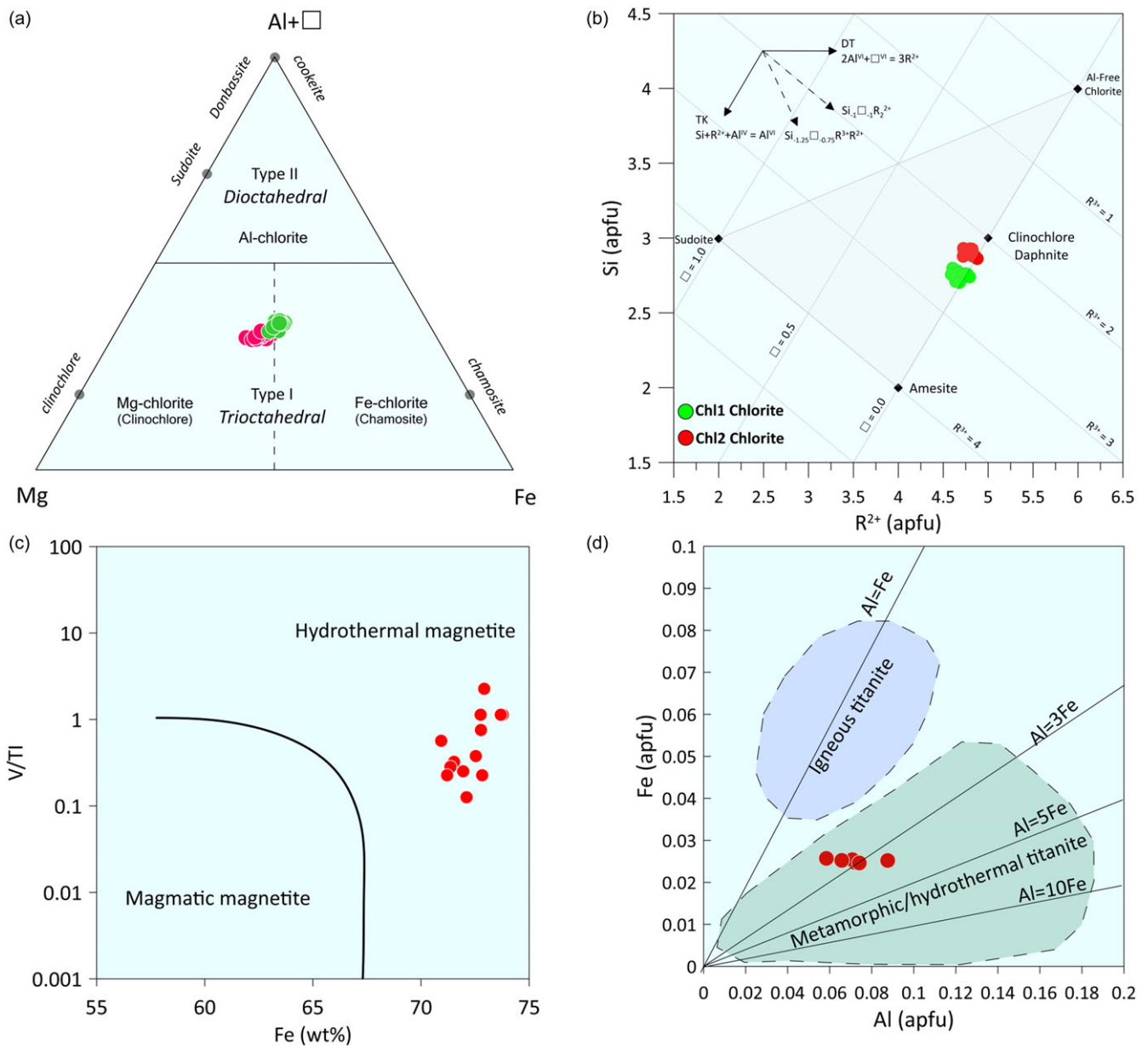


Figure 13. Diagrams showing the compositional variations of different minerals present in the alteration zone at Imalia. (a) $(Al + \square) - Mg - Fe$ compositional classification diagram for chlorite (According to Zane and Weiss 1998). \square represents structural vacancies. Grey circles represent end-members: clinochlore, chamosite, sudoite, and donbassite. Green circles represent Chl1 chlorite; red circles represent Chl2 chlorite. (b) Representation of compositional data set for chlorite in the $R^{2+} - Si$ diagram of Bourdelle and Cathelineau (2015). (c) A plot of Fe versus V/Ti for the magnetite from the Imalia deposit. (after Wen *et al.* 2017). (d) Classification diagram of titanite based on Al (pfu) versus Fe (pfu) composition. (modified after Ling *et al.* 2015, Kowallis *et al.* 2022).

line (TK) of Bourdelle and Cathelineau (2015) (Figure 13b). This parallelism suggests Tschermak substitution ($Al^{IV}Al^{VI} = Si$ (Mg, Fe^{2+})) in the Imalia chlorite.

At Imalia, magnetite remains the most important and ubiquitous oxide present in different ore types. Significant concentrations of this oxide were observed in the alteration zone. The analysed magnetite grains are mostly pure Fe_3O_4 , with trace amounts of Si, Mg, Mn, Ti and V. MnO content ranges from 0.04 to 0.3 wt%, while TiO_2 concentration ranges from 0.01 to 0.09 wt%. The Al_2O_3 concentration in the analysed magnetite was negligible. In the Fe, V/Ti plot of magnetite, the analysed grains fall into the hydrothermal field (Figure 13c).

Ilmenite is an important oxide present in several sections, mainly in the alteration zone, often alongside magnetite. The analysed ilmenite grains have TiO_2 content ranging from 51.2 to 55.5 wt%, while FeO content varies from 38.9 to 44.3 wt%. Significant amounts of MnO are present in the analysed ilmenite grains, ranging from 2.2 to 4.9 wt%, suggesting isomorphous substitution with pyrophanite ($MnTiO_3$) in the $FeTiO_3 - MnTiO_3$ solid solution.

Rutile has been observed primarily in the biotite-rich potassic zone, though it is also present in minor concentrations in the chlorite-rich zone. The TiO_2 content of rutile ranges from 98.8 to 99.3 wt%. The analysed grains have significant BaO, with

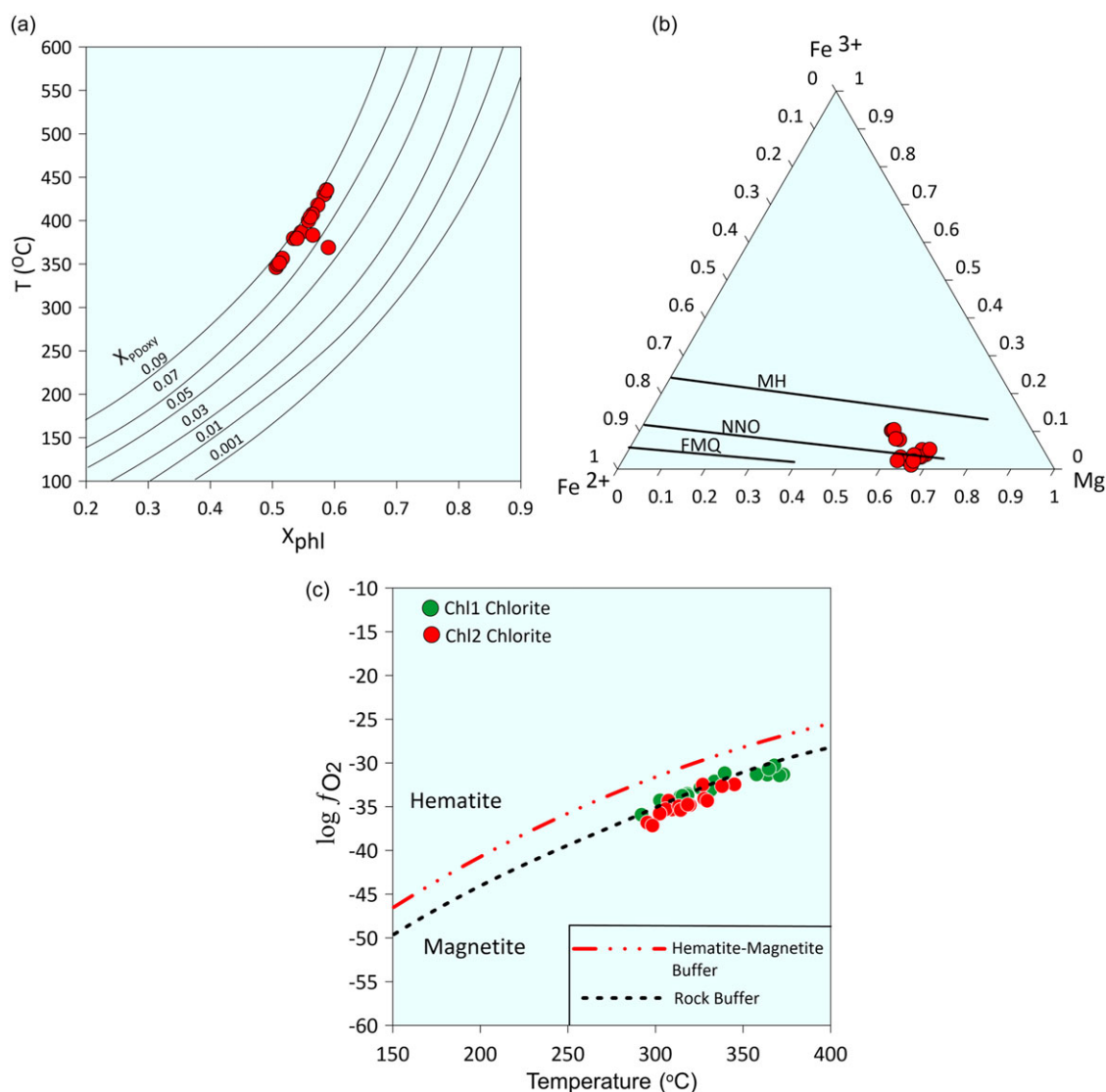


Figure 14. Diagrams showing the geothermometry of different minerals present in the alteration zone at Imalia. (a) Composition of biotite on X_{phl} versus temperature ($^{\circ}\text{C}$) diagram (modified from Beane, 1974). (b) Composition of biotite on Fe^{3+} - Fe^{2+} -Mg ternary diagram to estimate the oxygen fugacity (after Wones and Eugster, 1965). (c) Relationship between $\log f_{\text{O}_2}$ and temperature for chlorite samples. Most of the data fall within the magnetite stability field, closely aligned with the FMQ rock buffer curve. The boundaries defining the hematite-magnetite buffer and the rock buffer are based on the thermodynamic data of Lonker *et al.* (1990) and Giggenbach (1997), respectively.

concentrations ranging from 0.5 to 1.3 wt%, and minor amounts of FeO, with concentration ranging from 0.07 to 0.15 wt%.

Titanite is another dominant Ti-bearing phase present as distinctive elongated needle-shaped crystals mostly in the propylitic alteration zone. Titanite contains 36.2 to 37.7 wt% TiO_2 and 28.6 to 28.9 wt% CaO. The Fe/Al ratio varies from 0.29 to 0.44. In the Al-Fe plot of titanite, the analysed grains fall into the hydrothermal field (Figure 13d).

4.c. Geothermometry of minerals from the alteration zone

The composition of various silicates and oxides identified in the alteration zone can be used to estimate the thermometric conditions under which they formed. The temperature of formation for the Ca-amphiboles present in Imalia was estimated using the Ti-amphibole geothermometer of Liao *et al.* (2021),

which is specifically proposed for Ca-amphiboles. This geothermometer yielded temperature values ranging from 555 $^{\circ}\text{C}$ to 482 $^{\circ}\text{C}$, with a mean value of 520 $^{\circ}\text{C}$ for pargasite. For actinolite, the geothermometer provided temperatures between 386 $^{\circ}\text{C}$ and 320 $^{\circ}\text{C}$, with a mean value of 359 $^{\circ}\text{C}$. Beane (1974) proposed a geothermometer suitable for estimating the crystallisation temperature of hydrothermal biotite, particularly when biotite coexists with magnetite and K-feldspar. Since biotite in Imalia coexists with these minerals, its formation temperature was estimated using this geothermometer through Mica+ program (Yavuz, 2003). The calculated temperatures range from 436 $^{\circ}\text{C}$ to 346 $^{\circ}\text{C}$ (Figure 14a). Wones and Eugster (1965) suggested that the Fe^{2+} - Fe^{3+} -Mg ternary diagram for biotite can be used to determine oxygen fugacity. The composition of hydrothermal biotites in the alteration zone of the Imalia deposit falls at or above the FMQ (Fayalite-Magnetite-Quartz) and NNO (Nickel-Nickel Oxide)

Table 2. Summary of the geothermometric data for the minerals from the alteration zone in Imalia

| Type of Alteration Zone | Mineral | Temperature | $\log f_{O_2}$ |
|-------------------------|-----------------|-------------|-----------------------------|
| Potassic Alteration | Pargasite | 555–482°C | |
| Potassic Alteration | Biotite | 436–346°C | Between FMQ and NNO buffers |
| Potassic Alteration | Magnetite | 449–400°C | |
| Propylitic Alteration | Actinolite | 386–320°C | |
| Propylitic Alteration | Chlorite (Chl1) | 372–291°C | –30.3 to –34.3 |
| Propylitic Alteration | Chlorite (Chl2) | 345–282°C | –32.4 to –37.1 |
| Propylitic Alteration | Magnetite | 389–354°C | –30.9 to –32.7 |

buffers in the Fe^{2+} - Fe^{3+} -Mg diagram of Wones and Eugster (1965), indicating high oxygen fugacity (Figure 14b).

Chlorite thermometry has long been used to constrain the temperature of mineralising fluids in alteration assemblages, despite the lack of a buffering reaction (Essene, 2009). The chlorites from Imalia appear to be of hydrothermal origin. The analyses show (Na_2O+K_2O+CaO) contents of less than 0.5 wt.% and Ca concentration of less than 0.10 pfu, indicating the absence of other phyllosilicate intergrowths within the chlorite flakes (Cathelineau and Nieva, 1985), and thus, complete stoichiometry and suitability for thermometric studies. Consequently, commonly used empirical geothermometers were applied to determine the temperature of formation of hydrothermal chlorite. Although the chemistry of chlorite is influenced by factors such as fluid-to-rock ratio, oxygen and sulphur fugacities, pH, and the compositions of the host rock and hydrothermal fluid, which can affect the reliability of empirical geothermometers (e.g., Essene and Peacor, 1995; Essene, 2009), these methods have shown effective results (Klein *et al.* 2007) and remain widely used in alteration studies of ore deposit in low-grade rocks (e.g., Laverne *et al.*, 1995; Zang and Fyfe, 1995; Gillis *et al.* 2001; Timpa *et al.* 2005; Moura *et al.* 2006; Esteban *et al.* 2007). In this study, the chlorite geothermometers of Cathelineau (1988) (T1) and Jowett (1991) (T2) were used to estimate the temperature range for chlorite formation in the alteration zone. Additionally, Inoue *et al.* (2018) developed a semi-empirical formula that calculates relatively accurate temperatures for chlorite formation even when the Fe^{3+}/TFe pfu ratio is unknown. This formula, unlike other semi-empirical geothermometers that require these ratios, was also applied in the present study (T3). Since chlorite coexists with quartz and magnetite in the Imalia samples, we used a method proposed by Inoue *et al.* (2018), a simplification of the six-component solid solution model of Walshe (1986), to calculate $\log f_{O_2}$ using chlorite composition. Based on these geothermometers, the chlorite formation temperatures (T1–T3) for Chl1 range from 355–324°C, 360–330°C and 372–291°C, respectively, while the calculated temperatures for Chl2 range from 304–282°C, 307–286°C and 345–298°C, respectively. Overall, these different geothermometers provided temperature values ranging from 372 to 282°C for chlorite formation in Imalia. Similarly, the oxygen fugacity values calculated using the method suggested by

Inoue *et al.* (2018) for Chl1 ranged from $-30.27 \log f_{O_2}$ to $-34.3 \log f_{O_2}$. For Chl2, the oxygen fugacity values ranged from $-32.44 \log f_{O_2}$ to $-37.14 \log f_{O_2}$. The calculated $\log f_{O_2}$ values were plotted as a function of formation temperature. Both chlorites plot below the hematite–magnetite equilibrium curve, closely aligning with the FMQ rock buffer curve (Figure 14c).

The composition of magnetite, an important oxide phase present in the alteration zone, also provided crucial geothermometric information. The T_{Mg-Mag} geothermometer of Canil and Lacourse (2020) was used to calculate the temperature of magnetite crystallisation from the potassic and propylitic alteration zones. Magnetite from the potassic alteration zone showed an average temperature of 425°C, while magnetite from the propylitic alteration zone had an average temperature of 377°C. Similarly, the coexisting assemblage of magnetite and ilmenite from the propylitic alteration zone, using the geothermometry of Anderson and Lindsley (1985), yielded an average temperature of 362°C and a mean oxygen fugacity of $-32 \log f_{O_2}$. A summary of the geothermometric data from the minerals of the alteration zone is provided in Table 2.

5. Discussion

The present study, based on a detailed account of the nature of hydrothermal alteration and its mineral chemistry, aims to reconstruct the sequence of hydrothermal events that altered the host rocks of the Imalia area and to characterise the fluids and physico-chemical conditions prevailing before and during the polymetallic mineralisation.

5.a. Progressive transformation of hydrothermal system: Insights from alteration geochemistry and mineral paragenesis

The stage for the polymetallic mineralisation of type 3 and type 4 ore at Imalia was set by the emplacement of quartz porphyry dykes. The shallow intrusion of the porphyry body is indicated by the development of quartz eyes in a fine-grained sericitised quartzose groundmass of the porphyry samples (Tripathi, 2008). This intrusion initiated hydrothermal activity that interacted with the carbonate host lithology. The precipitation of medium- to small-grained subhedral hydrothermal amphiboles, pargasite in composition, appears to be an initial product of this interaction, present in small amounts in a few samples along with quartz and rare pyrite and rutile grains. The geothermometric data for these amphiboles (Table 2) is consistent with the fluid inclusion data from type 3 ore, which indicate a peak temperature of 509°C, supporting the petrographic observation that these hydrothermal Ca-amphiboles formed during the initial phase of hydrothermal activity. In these initially formed ores, rare fine- to medium-grained garnets were also identified. The very low TiO_2 concentration of garnet in Imalia imply high activity of SiO_2 during their formation (Dingwell and Brearley 1985). Unlike igneous garnets, these low TiO_2 concentration support their hydrothermal origin, aided by metasomatic action in the alteration halo (Huggins *et al.* 1977; Deer *et al.* 1992).

The formation of these initial silicate minerals was followed by the precipitation of a substantial amount of hydrothermal biotite, accompanied by K-feldspar, magnetite, rutile, quartz, apatite and pyrite grains. The observation of high f_{O_2} and high-temperature hydrothermal fluid responsible for the precipitation of this biotite (Table 2) is further supported by its low $Fe/(Fe + Mg)$ ratio (Richards 2011; Dilles 1987). Along with biotite, the development

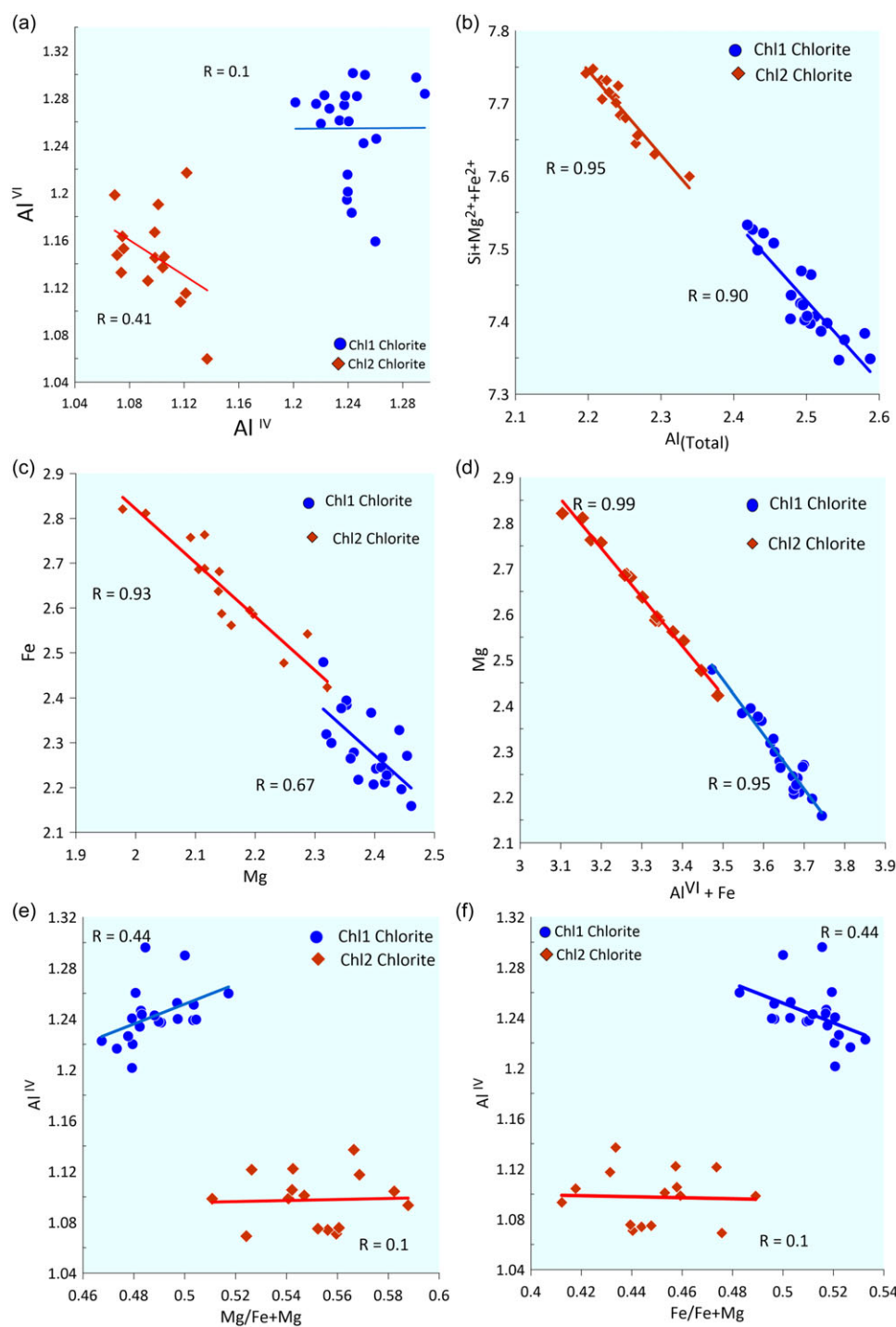


Figure 15. Binary diagrams showing the statistical correlation between main cations of chlorite in Imalia. (a) Al^{IV} versus Al^{VI} , (b) $Si+Mg+Fe$ versus Al^{Total} , (c) Mg versus Fe , (d) $Al^{VI} + Fe$ versus Mg , (e) $Mg/Fe+Mg$ versus Al^{IV} and (f) $Fe/Fe+Mg$ versus Al^{IV} .

of K-feldspar and rutile also supports high-temperature hydrothermal activity enriched in K at the initial phase of wall rock interaction at approximately 425°C (e.g., Robb, 2005; Bodnar *et al.* 2014; Pacey *et al.* 2020). This initial potassic-rich phase is followed by a more prominent propylitic alteration halo. Outward movement and cooling of hydrothermal fluid, with declining aqueous K^+ and increasing H^+ , explain this alteration pattern. In distal areas, where H^+ metasomatism becomes dominant, a decline in fluid-to-rock ratio and reaction with Ca-Mg-rich carbonate minerals may have resulted in a widespread propylitic alteration

halo. This extensive alteration zone, consisting mainly of chlorite, epidote, ankerite, siderite, albite, titanite, actinolite and rare calcite, indicates formation at temperatures below 350°C (Cho and Liou, 1987).

Chlorite is a key silicate of this propylitic alteration phase. Chlorite geothermometry from the propylitic zone yields a temperature range between 280°C and 370°C, which is well within the temperature range calculated for type 3 ore from fluid inclusion data. Petrographic evidence suggests that there are two types of chlorite present in Imalia: Ch1, formed directly from

hydrothermal fluid, and Chl2, which replaced earlier precipitated biotite. Both types are trioctahedral and fall within the clinocllore series. Trioctahedral chlorite is commonly associated with hydrothermal systems (Shikazono and Kawahata, 1987). Three ion substitution mechanisms for chlorite have been proposed, depending on pressure, temperature, chemical compositions of the host rock, and physicochemical conditions of the hydrothermal environment (Inoue *et al.* 2010; Zhang *et al.* 2020 and references therein):

(1) $\text{Fe}^{2+} \Leftrightarrow \text{Mg}^{2+}$, (2) Tschermak Al^{IV} and $\text{Al}^{\text{VI}} \Leftrightarrow \text{Si}$ (Mg^{2+} , Fe^{2+}), and (3) di-trioctahedral $3(\text{Mg}^{2+}$, $\text{Fe}^{2+}) \Leftrightarrow \square + 2 \text{Al}^{\text{VI}}$. The concentration of Al^{IV} and Al^{VI} help understand the substitutional relationship between octahedral and tetrahedral positions of chlorite. For both Chl1 and Chl2 chlorites (Figure 15a), Al^{IV} shows no correlation with Al^{VI} , suggesting that the di-trioctahedral substitution ($3(\text{Mg}^{2+}$, $\text{Fe}^{2+}) \Leftrightarrow \square + 2 \text{Al}^{\text{VI}}$) is likely not significant (Xie *et al.* 1997). The Al_{total} concentration shows a good negative correlation with the ($\text{Si} + \text{Fe}^{2+} + \text{Mg}^{2+}$) concentration (Figure 15b), indicating complete Tschermak substitution in Imalia chlorite. Similarly, the Fe^{2+} concentration of Imalia chlorite exhibit a good negative correlation with Mg (Chl1, $R = 0.67$, and Chl2, $R = 0.93$), suggesting that Mg^{2+} and Fe^{2+} replacement is predominant in the octahedral position (Xie *et al.* 1997) (Figure 15c). In the Mg-(Fe + Al^{VI}) diagram (Figure 15d), both Chl1 and Chl2 chlorites show a strong negative correlation (Chl1, $R = 0.99$, and Chl2, $R = 0.95$), indicating that Fe and Al^{VI} predominantly substitute Mg in the octahedral position. The relationship between $n(\text{Al}^{\text{IV}}) - n(\text{Mg})/n(\text{Fe} + \text{Mg})$ and $n(\text{Al}^{\text{IV}}) - n(\text{Fe})/n(\text{Fe} + \text{Mg})$ in Imalia (Figures 15e,f) shows a weak correlation for both chlorites. This suggests that, with the replacement of Si by Al^{IV} in the tetrahedral position, Mg is also replaced by Fe in the octahedral position, resulting in a slight increase in Fe content and a corresponding decrease in Mg content in Imalia chlorite (cf. Xie *et al.* 1997). Studies indicate that Fe substitution for Mg mainly occurs in acidic conditions, whereas a relatively alkaline environment favours Mg substitution for Fe (Cathelineau, 1988; Yuan *et al.* 2018). This suggests that chlorites in the Imalia deposit formed in a relatively acidic environment. The Fe/Fe+Mg ratio is crucial for understanding the nature of the hydrothermal fluid. For Chl1 chlorite, the ratio ranges from 0.52 to 0.48, while for Chl2 chlorite, the values range from 0.49 to 0.41. This indicates a gradual decrease in Fe/Fe+Mg from Chl1 to Chl2 chlorite, suggesting an increasing role of meteoric water in the fluid system during the formation of Chl2 chlorite, which also decreased the overall temperature of the hydrothermal fluid.

The metasomatic textures and the altered chlorite retaining the original biotite grain shape suggest that Chl2 chlorite formed by replacing the micaceous mineral. Xiao and Huayong (2020) proposed that elemental transfer during the alteration process, in this case from biotite to chlorite, could be determined using electron probe data for both minerals, alongside the role of the hydrothermal fluid. Using the equation and method they suggested, the elemental transfer from biotite to chlorite was calculated. Data greater than 100% indicate contributions from the hydrothermal fluid. In Chl2, SiO_2 (avg. 48%), Al_2O_3 (avg. 88%), FeO_T (avg. 106%), MgO (avg. 74.5%) and MnO (avg. 272%) were introduced during the conversion from biotite. Jiang and Peacor (1994) demonstrated that biotite is altered to chlorite mainly through a layer-by-layer replacement mechanism, characterised by metasomatic textures similar to those observed at Imalia (Figures 6g, h). Two chloritization mechanisms are proposed for this layer-by-layer replacement: 1Bt \rightarrow 1Chl, which involves a

significant inflow of metallic ions (Al^{3+} , Fe^{2+} and Mg^{2+}) from the hydrothermal fluid into an octahedral sheet in chlorite, and 2Bt \rightarrow 1Chl, involving little or no inflow of metallic ions from the hydrothermal fluid (Eggleton and Banfield, 1985; Yuguchi *et al.* 2015; Xiao and Huayong, 2020). In the case of 1Bt \rightarrow 1Chl, a large amount of Al is required to be introduced into chlorite. Since no Al is introduced during the formation of Chl2 chlorite, and most of the Al is conserved in the biotite-chlorite system during chloritization, which is consistent with previous studies that Al is less mobile in fluids (Shriver and Maclean, 1993), the 2Bt \rightarrow 1Chl mechanism appears more plausible than 1Bt \rightarrow 1Chl. While all Fe and Mn from biotite entered chlorite during alteration, there was also a moderate influx of Fe (+6%) and a significant contribution of Mn from the hydrothermal fluid (+172%). A small amount of Mg and abundant Si and Ti were lost during chloritization, further supporting the 2Bt \rightarrow 1Chl mechanism. Petrographic evidence shows that abundant quartz formed during the chloritization of biotite, as indicated by its increasing concentration close to Chl2 chlorite samples. This suggests the outflow of considerable amounts of Si during chloritization, consistent with the 2Bt \rightarrow 1Chl mechanism rather than the 1Bt \rightarrow 1Chl mechanism. Additionally, the absence of deformation in the chloritised biotite rules out the 1Bt \rightarrow 1Chl mechanism (Chayes, 1955; Eggleton and Banfield, 1985; Yuguchi *et al.* 2015). A small amount of Mg that outflowed toward the hydrothermal fluid resulted in Mg-rich carbonates around chloritised samples (Tripathi, 2008). Most of the potassium in biotite, released during chloritization, was removed by the hydrothermal fluids. Thus, it appears that at Imalia, Chl2 chlorite formation occurred through the 2Bt \rightarrow 1Chl mechanism, depending on the availability and supply of metallic ions from the hydrothermal fluid (Figure 16a).

The composition of epidote, an important constituent of the propylitic phase of alteration, also provides significant information about the oxidising conditions during its precipitation. The Ps value of epidote is strongly dependent on the oxidation state of iron and is represented by $\text{Fe}^{3+} \Leftrightarrow \text{Al}^{3+}$ substitution (Bird and Spieler, 2004). Increasing oxidation causes a higher $[\text{Fe}^{3+}]$ concentration in hydrothermal fluid that substitutes Al^{3+} , resulting in a higher Ps value in epidote (Beaufort *et al.* 1992). The calculated epidote Ps values from Imalia range from 12 to 27. This suggests that the epidotes are more aluminous, formed at lower temperatures, and underwent significant fluctuations in the $f\text{O}_2$ of fluid during propylitic alteration. Actinolite is also present in small amounts along with chlorite and epidote in the propylitic alteration zone. The geothermometric data for actinolite indicate a mean formation temperature of 359°C (Table 2). Jenkins and Bozhilov (2003) experimentally constrained the thermal stability of actinolite between 350°C to 480°C at a maximum of 2 kbar pressure. They showed that grunerite begins to nucleate by replacing actinolite above 2 kbar. The absence of grunerite in Imalia and the mean temperature of actinolite formation at 359°C, near the lower end of its thermal stability, constrain the pressure to approximately 1 kbar or less during actinolite precipitation. (Figure 16b).

Magnetite is the most important oxide mineral present in both the potassic and propylitic alteration phases. According to Nadoll *et al.* (2014), the concentration of Al and Ti, among other elements, helps identify the source of magnetite. While igneous magnetite has high Al_2O_3 and TiO_2 content, hydrothermal magnetite typically has lower or insignificant amounts of these elements. The magnetite at Imalia has negligible amounts of both, indicating a hydrothermal origin. Texturally and compositionally, the magnetite in potassic and propylitic alteration phases differs

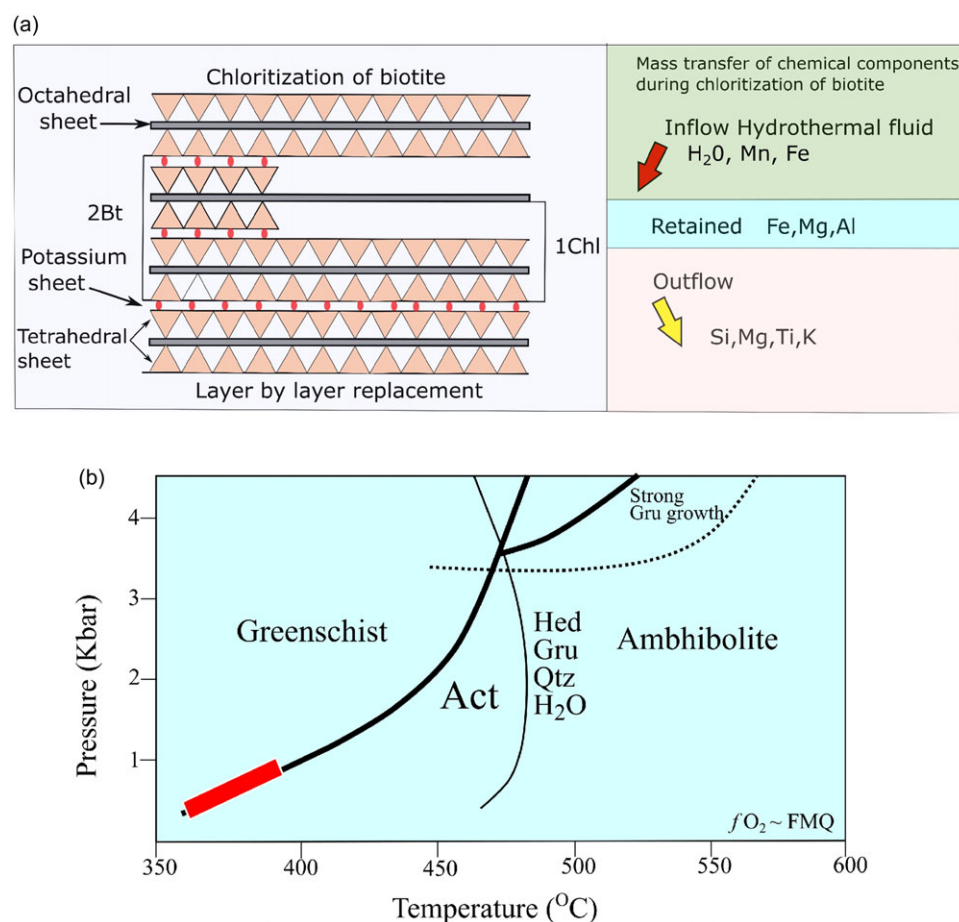


Figure 16. (a) Schematic figure showing the development of crystal chemistry and mass transfer of chemical components in the chloritization process of biotite. (modified after Yuguchi *et al.* 2015; Xiao and Huayong, 2020). (b) Pressure–temperature diagram showing the most likely condition under which actinolite formed at Imalia. The thermal stability of actinolite is experimentally constrained to be between approximately 350°C at 480°C. Above 2 kbars, actinolite is replaced by grunerite (Jenkins and Bozhilov, 2003). The red bar indicates the temperature and pressure range of actinolite formation in Imalia (diagram modified after Jenkins and Bozhilov, 2003). Abbreviations: Act – Actinolite, Gru – Grunerite, Hed – Hedenbergite, Qtz – Quartz.

slightly. Magnetite in the potassic-rich zone exhibits a smooth texture and subhedral to euhedral grain characteristics, with relatively higher contents of trace elements such as Si, Ti, Mg and Al. The elevated concentrations of these trace elements suggest increased fluid-rock interaction during the initial hydrothermal activity in Imalia. These magnetite grains also developed fractures in places, possibly caused by later fluid metasomatism. In contrast, magnetite in the propylitic zone, found in close proximity to chlorite and epidote, is highly fractured, porous in places and some show compositional zoning. Ilmenite exsolution lamellae can also be observed in these magnetites.

The presence of porosity in propylitic stage magnetite and the reduction in trace element concentration, especially Ti, Mg, Si and Al, suggest that some of these elements were generated by a coupled dissolution-precipitation (CDR) mechanism. At Imalia, hydrothermal alteration occurred in carbonate lithology, and the dissolution of carbonate host rocks caused disequilibrium between precipitated magnetite and residual hydrothermal fluid, resulting in the CDR reaction. Additionally, the gradual decrease in temperature and the injection of high-salinity fluid, as evidenced by fluid inclusion data, along with volume changes, facilitated the formation of porous magnetite via the CDR process. Compositional variations in some magnetite grains, such as oscillatory zoning, may be due to crystallisation from fluids with fluctuating elemental conditions (Deditius *et al.* 2018; Shore and Fowler, 1996). These magnetite grains were replaced by hematite

and titanite in several places, providing two important clues: first, that this magnetite underwent hydrothermal metasomatism, and second, that the early hydrothermal fluid responsible for the alteration zone was highly oxidised. The gradual drop in Ti content in magnetite from the potassic alteration phase to the propylitic zone at Imalia indicates a continuous decrease in hydrothermal temperature, a conclusion supported by data from other silicates. Similarly, the low V content in Imalia magnetite, with some values even below the detection limit in EPMA studies, indicates a high oxygen fugacity environment (Acosta-Gongora *et al.* Acosta-Góngora *et al.*, 2014). Mn in magnetite is a redox-sensitive element (Toplis and Corgne, 2002), and variations in Mn content in Imalia magnetite suggest significant fluctuations in oxygen fugacity during its precipitation. The relative enrichment of Mn in magnetite from the propylitic stage supports the notion that these formed at low temperatures, based on thermodynamic studies by Ilton and Eugster (1989) and Wu *et al.* (2019), which showed that Mn preferentially partitions into magnetite at low temperatures in Cl-rich fluids

As mentioned earlier, titanium minerals that include rutile, titanite, and ilmenite are present in small amounts in the Imalia alteration zone. Titanium is generally considered an immobile element that gets incorporated in the alteration zone by replacing earlier Ti-rich minerals. The absence of Ti-rich minerals in the host lithology in Imalia, but their presence in the alteration zone, suggests that it is the hydrothermal fluid that brought titanium

with it. Studies indicate that titanium can be transported in hydrothermal fluids at high temperatures due to its increasing solubility in volatile-rich aqueous fluids in the form of chlorides, fluorides, hydroxides, or other complexes, thus enhancing its mobility (Rabbia *et al.* 2009; Czamanske *et al.* 1981). The involvement of fluorine-rich fluids at Imalia is suggested by the presence of fluorite in the porphyry dyke samples and a minor amount in the alteration zone, as well as apatite, another F-containing silicate, in the potassic-rich zone (GSI unpublished report). This indicates that the hydrothermal fluid at the initial stage was not only high in temperature and highly oxidised but also volatile-rich, which increased the solubility of titanium and its transportation by the hydrothermal fluids (Gieré, 1986; Jiang *et al.* 2005; Rabbia *et al.* 2009)—the reason for the presence of rutile, titanite and ilmenite in the Imalia ore. Additionally, during the later stage of propylitic alteration, some titanium was released during the breakdown of biotite, contributing to the formation of ilmenite and titanite, which are present in the chlorite-magnetite-rich samples. The TiO₂ concentration (36.2–37.7 wt%) and Al₂O₃ + FeO concentration (2.4–3.2 wt%) of titanites from Imalia are consistent with their hydrothermal origin (e.g., Xie *et al.* 2018; Xiao *et al.* 2020) (Figure 13d). The low Fe/Al ratio (average 0.36) in the studied titanite further supports the estimation of high *f*O₂ conditions of the hydrothermal fluid during their precipitation (Celis, 2015).

Since carbonate rocks constitute the bulk of the host lithology, they underwent significant changes during the alteration phase. Carbonatization in Imalia produced ankerite, siderite, ferro-dolomite, and a small amount of calcite, indicating an increased input of Fe, Mn, and Ca from the hydrothermal fluid. Ankerite and siderite are more widespread in the proximal zone of mineralisation, while ferro-dolomite is more commonly found in the distal part, often associated with sericite-rich phyllic phases. Calcite is present in small amounts within a biotite-rich assemblage and in propylitic and phyllic phase minerals formed at a later stage of alteration.

The hydrothermal activity in Imalia resulted in extensive silicification of the host dolostone in the mineralised zone. The megascopic and mesoscopic evidence of silicification includes the spread of jasperoidal masses, a product of hydrothermal metasomatic activity replacing carbonates (Lovering, 1962), along with quartz veins in the mineralised zone; most of these veins align with the direction of the shear zone in Imalia. Additionally, a sizeable amount of sulphides is present in close association with these quartz veins. Petrographic studies of the quartz veins show fibrous and comb textures, supporting the shallow origin of the vein-type mineralisation. The presence of boudins and sigmoidal veins, some infilled with sulphides, suggests increasing shearing influence during the mineralisation event. The subsequent hydrothermal brecciation of these quartz veins and the host carbonate rocks, resulting in different types of breccia, indicates their formation under low-pressure conditions (1–2 kbar, e.g., Jébrak, 1997; Torresi *et al.* 2012) within a brittle deformation zone (<10 km, Davis *et al.* 2012).

Sericite is an important silicate present in the alteration zone at Imalia. A small concentration of sericite in the potassic zone samples appears mostly as a replacement of K-feldspar, indicating a later overprinting episode. This micaceous mineral is also present in small amounts with the propylitic alteration phase minerals. However, petrographic evidence shows that sericite becomes the dominant silicate during the supergene stage, alongside quartz and

a small amount of calcite, barite, and hematite. The martitization of earlier precipitated magnetite into hematite (Figure 7i) points to the gradual oxidation of fluid and cooling of the hydrothermal system. This is further supported by fluid inclusion data showing that, at a later stage of mineralisation, inclusions are dominated by low-temperature (<200°C) fluids, predominantly of lower salinity (<10 wt.% NaCl equivalent) due to the addition of meteoric water, possibly in a brittle deformation regime.

5.b. Implication for ore genesis

In its initial phase, hydrothermal activity in Imalia caused extensive alteration of the host lithology. During this phase, the magma-derived fluids were not only of high temperature and were highly oxidised but also volatile-rich, which facilitated the formation of various potassic-rich silicates and oxide minerals. This was followed by a propylitic alteration phase, marked by the precipitation of silicates and oxides at cooler temperatures. Geothermometric data from minerals in the propylitic zone indicate formation temperatures of approximately 250°C to 370°C, which are significantly lower than those in the potassic alteration stage. This temperature difference suggests that the hydrothermal system cooled over time and/or experienced upward and outward fluid circulation. Borehole data, petrographic evidence and mineral paragenesis support this scenario of initial high-temperature hydrothermal fluids creating the potassic zone, followed later by cooler (<370°C) fluids. This shift led to extensive propylitic alteration in both proximal and distal zones, with an increasing influence of meteoric water. This alteration involved an alkali exchange, characterised by increases in Na, Ca, Mn and K, along with variable changes in Mg and Si. The hydrothermal alteration also modified the physicochemical properties of the host carbonate rocks, significantly increasing their porosity and permeability. These changes enhanced reactions between hydrothermal fluids and the wall rock during the pre-metallogenic stage, creating favourable conditions for polymetallic mineralisation due to the more fragile and permeable nature of the altered wall rocks.

Evidence of extensive brecciation in a brittle regime at Imalia, likely related to over-pressured hydrothermal fluids, caused hydraulic disaggregation of the host rocks, leading to the formations of various types of breccias. These breccias, often rich in sulphides, may have played a crucial role in the deposition of gold during the main mineralisation stage at Imalia. Studies have shown that a sharp drop in pressure in a shallow environment is more likely to cause extensive boiling (Cunningham, 1978), as also indicated by the fluid inclusion data from the alteration zone at Imalia. As the hydrothermal fluid ascended to shallower levels, rapid boiling occurred, facilitating intense brecciation and pressure release, which is a useful mechanism for gold deposition, as the abrupt loss of H₂S destabilises the bisulphide complexes responsible for transporting gold in epithermal systems.

Studies have shown that oxygen fugacity generally decreases away from magmatic-hydrothermal systems as oxidised fluids are progressively reduced by interaction with country rocks (Cooke *et al.* 2014). However, at Imalia, a relatively high *f*O₂ is implied due to the significant concentrations of magnetite, hematite, and epidote throughout the alteration zone surrounding the sulphide mineralisation. This consistent high oxidation state of the hydrothermal fluid is attributed to the decrease in pressure as the hydrothermal fluid moved toward shallower depths. This resulted in the escape of H₂ and the subsequent dissociation of

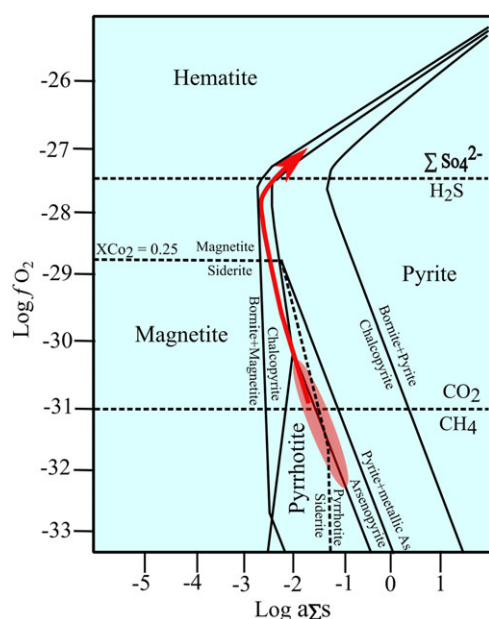


Figure 17. Log $a\Sigma s$ versus log fO_2 showing the stability fields for iron sulphides and oxides from Imalia (modified from Mikucki and Ridley, 1993; calculated at $T = 350^\circ\text{C}$, $P = 2$ kbar, and $\Sigma\text{SO}_4 = 10^3 a_{\text{SO}_4^{2-}}$). The magnetite–pyrite–chalcopyrite of type 3 ore occurs under high fO_2 conditions. The red ellipse area delineates the approximate conditions for the formation of the type 3 ore, while the red arrow shows the oxidation trend during the mineralisation.

H_2O , along with an increase in fO_2 (Proffett, 2003; Brimhall and Crerar, 1987; Dilles, 1987). The process of separation of sulphur from the magma can also lead to oxidation under subsolidus magmatic-hydrothermal conditions. As water saturation occurs during magmatic crystallisation, sulphur, primarily as $\text{SO}_2 > \text{H}_2\text{S}$ at magmatic T - fO_2 , preferentially partitions into the aqueous fluid phase. This process during cooling leads to reactions, such as, $\text{SO}_2(\text{aq}) + \text{H}_2\text{O}(\text{aq}) = \text{H}_2\text{S}(\text{aq}) + \frac{3}{2} \text{O}_2(\text{g})$ (Dilles, 1987). The removal of sulphur as metal sulphides from the aqueous fluid would, therefore, cause oxidation of magmatic Fe-Mg silicates and Fe-Ti oxide assemblages. A phase diagram showing changes in the oxidation state during the formation of the alteration halo based on the mineralogical assemblage at Imalia is presented in Figure 17. It appears that the continuous crystallisation of magnetite from the potassic to propylitic alteration in Imalia reduced the environment, resulting in changes in oxygen and sulphur fugacities, providing a suitable platform for later sulphide precipitation. During the transition from potassic to propylitic and subsequently to sericite alteration, the hydrothermal fluid compositions evolved by decreasing $\log(\alpha\text{K}/\alpha\text{H}^+)$ values, reducing the stability of metal complexes with bisulphide, chloride and other ligands, ultimately causing abundant precipitation of sulphide minerals and the replacement of secondary K-feldspar and plagioclase with sericite (Brimhall and Crerar, 1987; Seo *et al.* 2009; Mountain and Seward, 2003; Seedorff *et al.* 2005). A schematic diagram showcasing various stages of hydrothermal alteration followed by vein-type mineralisation at Imalia is presented in Figure 18.

6. Conclusions

1. The polymetallic vein-type mineralisation at Imalia took place along an approximately 1.5 km-long, ENE-WSW-

trending, intermittent shear zone within carbonate host rocks, following the emplacement of quartz porphyry dykes in the region. Hydrothermal fluids during its interaction with the carbonate lithology precipitated sulphides and various silicate minerals, creating a complex alteration halo.

2. Hydrothermal Ca-amphiboles, along with a minor amount of garnet, were the first silicates to form at around 500°C . This was followed by the precipitation of the potassic phase of biotite, K-feldspar, as well as apatite, rutile, pyrite, magnetite and calcite.
3. A subsequent lower-temperature pulse of hydrothermal fluid overprinted the earlier silicates, forming a propylitic alteration halo with abundant chlorite, epidote, albite, actinolite, sericite, calcite, magnetite, ilmenite and titanite, followed by vein-type sulphide mineralisation. Phyllic and argillic alterations in the supergene stage included kaolinization, limonitization and malachitization.
4. Chloritization and epidotization are the most widespread alterations, forming extensive alteration halos around the orebody. Among the two types of chlorite present in Imalia, Chl1 formed directly from the hydrothermal fluid during the initial phase of hydrothermal activity, while Chl2 appears to have formed slightly later by replacing earlier precipitated biotite through a layer-by-layer replacement mechanism ($2\text{Bt} \rightarrow 1\text{Chl}$). Most of the chlorite formed under a high water/rock ratio with increasing meteoric water influence. Magnetite, an important oxide phase in the alteration zone, is highly fractured in places. Some magnetite in the propylitic alteration zone is porous and may have precipitated via a coupled dissolution-precipitation process.
5. Brecciation in the ore zone at Imalia occurred in a brittle regime and is linked to overpressured fluids that caused the hydraulic disaggregation of the host rocks, resulting in different types of breccia infilled with silicates and leading to extensive sulphide mineralisation.
6. Geothermometric and fluid inclusion data suggest that alteration zone minerals formed within a temperature range of approximately 150°C to 550°C , at pressures around 1 kbar and depths of less than 10 km, with an average oxygen fugacity of $\log -32$.
7. The data from the silicates and oxides present in the alteration zone reveal evolving fO_2 conditions. Biotite, which precipitated at an earlier stage, exhibits fO_2 values at or above the FMQ and NNO oxygen buffers. Chlorite, key constituents of the propylitic stage, display fO_2 conditions near the FMQ oxygen buffer. The composition of other silicates present in the alteration zone supports this inference. During the main sulphide mineralisation stage, oxygen fugacity increased further with the rising influence of meteoric water, as indicated by fluid inclusion data, magnetite martitization, the presence of arsenian pyrite (Tripathi and Deb, 2022), and the near-complete martitization of magnetite during the supergene stage.
8. The hydrothermal silicate minerals precipitated during the development of the alteration zone record the transition of the hydrothermal fluid from a brittle-ductile to a dominantly brittle structural regime, related to episodic decompression due to fluid overpressuring and hydrofracturing. Early potassic phase alteration involved infiltration of hydrothermal fluids along fine fractures at carbonate grain

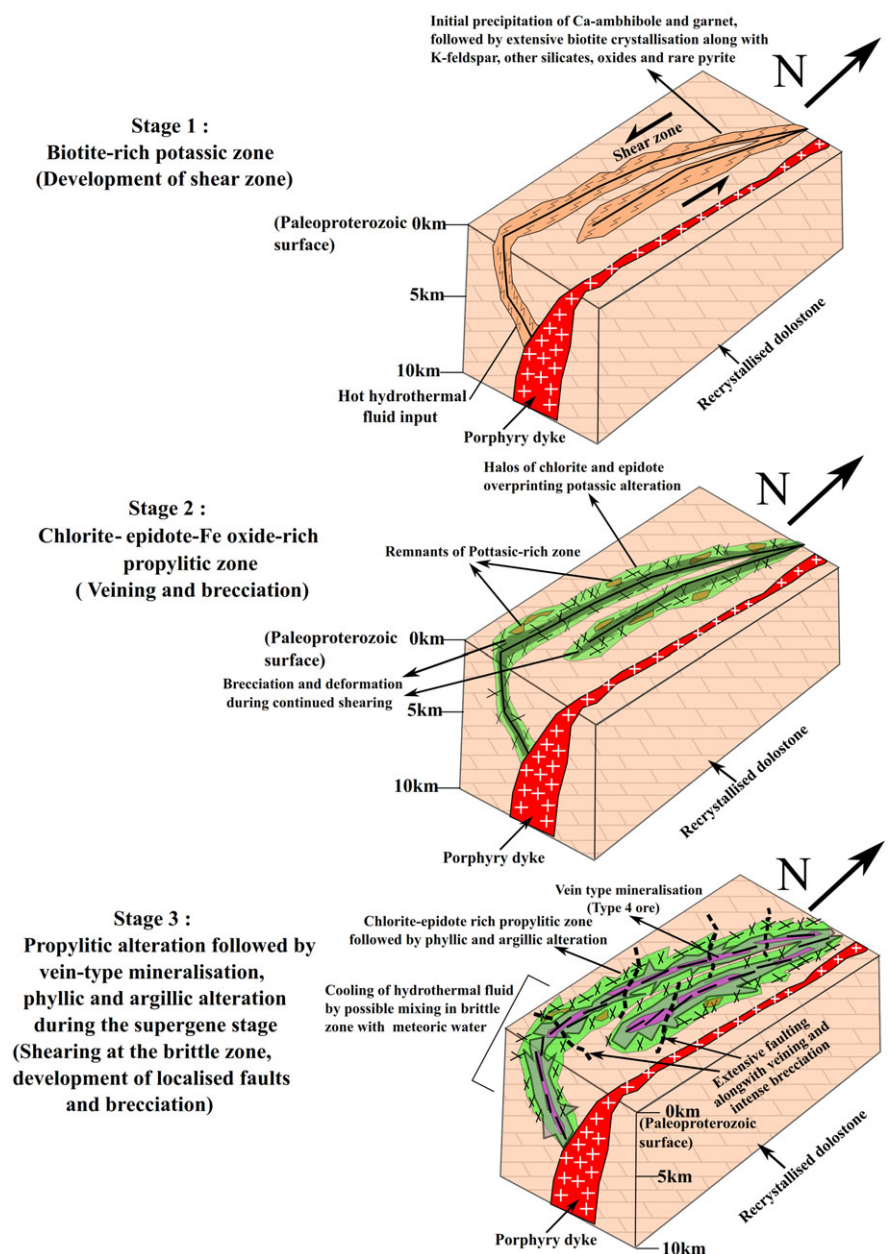


Figure 18. Schematic model illustrating the interpreted evolution of the Imalia deposit in the context of hydrothermal alteration associated with silicate, carbonate and oxide-rich phases and subsequent sulphide mineralisation.

boundaries. Later, pervasive propylitic alteration was influenced by shear zone development. Fluid flow related to these alteration stages appears to have been controlled by permeability in shear zones, enhanced by interconnected small fractures and fault planes. The sulphide mineralisation stage occurred under brittle conditions, an inference supported by fluid inclusion data and the presence of open-space filling textures associated with vein-type mineralisation.

- Overall, we propose that hydrothermal activity at Imalia, following quartz porphyry dyke emplacement, occurred at a shallow depth in a brittle-ductile regime. Initial high-temperature, volatile-rich hydrothermal fluids interacted with the host carbonates to form a complex alteration halo. Subsequently, with the involvement of metal-rich low-temperature hydrothermal fluid that started mixing with

the meteoric fluids in the brittle deformation zone, combined with significant fluctuations in fO_2 conditions and a decrease in temperature and salinity, ideal conditions for vein ore deposition were established at Imalia.

Supplementary material. The supplementary material for this article can be found at <https://doi.org/10.1017/S0016756825000056>

Acknowledgements. The first author is thankful to CSIR, Government of India, for financial support in the form of a Senior Research Fellowship. This research, however, did not receive any specific grant from funding agencies in the public, commercial, or not-for-profit sector. We express our gratitude to GSI for providing access to the borehole cores and some of their unpublished reports. Thanks are due to GSI, Faridabad, and the National Centre of Mineralogy, Prayagraj, for their help in generating the EPMA data used in this study. The first author also expresses gratitude to his parents, Dr. Krishna Nidhi Tripathi and Mrs. Anjana Tripathi, for their support throughout this work. We

thank Dr. Eleanor Jennings for her suggestions which significantly improved the presentation.

Competing interests. The authors declare that they have no known competing financial interests or personal relationships that could have appeared to influence the work reported in this paper.

References

- Acharyya S and Roy A** (2000) Tectonothermal history of the central Indian tectonic zone and reactivation of major faults/shear zones. *Journal Geological Society of India* **55**, 239–256.
- Acosta-Góngora P, Gleeson SA, Samson IM, Ootes L and Corriveau L** (2014) Trace element geochemistry of magnetite and its relationship to Cu-Bi-Co-Au-Ag-U-W mineralization in the Great Bear magmatic zone, NWT, Canada. *Economic Geology* **109**(7), 1901–1928.
- Andersen DJ and Lindsley DH** (1985) New (and final!) models for the Ti-magnetite/ilmenite geothermometer and oxygen barometer. *Abstract AGU 1985, Spring Meeting Eos Transactions American Geophysical Union* **66**(18), 416.
- Beane RE** (1974) Biotite stability in the porphyry copper environment. *Economic Geology* **69**, 241–256.
- Beane RE and Titley SR** (1981) Porphyry copper deposits Part II Hydrothermal alteration and mineralization. *Economic Geology 75th Anniversary volume*, 235–269.
- Beaufort D, Patrier P, Meunier A and Ottaviani MM** (1992) Chemical variations in assemblages including epidote and/or chlorite in the fossil hydrothermal system of Saint Martin (Lesser Antilles). *Journal of Volcanology and Geothermal Research* **51** (1–2), 95–114.
- Beaufort D, Rigault C, Billon S, Billault V, Inoue A, Inoue S and Patrier P** (2015) Chlorite and chloritization processes through mixed-layer mineral series in low temperature geological systems – a review. *Clay Mineral* **50**, 497–523.
- Bird DK and Spieler AR** (2004) Epidote in geothermal systems. *Reviews in Mineralogy and Geochemistry* **56** (1), 235–300.
- Bodnar RJ, Lecumberri-Sanchez P, Moncada D and Steele-MacInnis M** (2014) Fluid inclusions in hydrothermal ore deposits. In *Treatise on Geochemistry* (eds HD Holland, & KK Turekian), 13, pp 119–142. Second Edition, Oxford: Elsevier.
- Bodnar RJ, Reynolds TJ and Kuehn CA** (1985) Fluid-inclusion systematics in epithermal systems. *Reviews in Economic Geology* **2**, 73–97.
- Bora S and Kumar S** (2015) Geochemistry of biotites and host granitoid plutons from the Proterozoic Mahakoshal Belt, central India tectonic zone, implication for nature and tectonic setting of magmatism. *International Geology Review* **57**(11–12), 1686–1706.
- Bourdelle F and Cathelineau M** (2015) Low-temperature chlorite geothermometry, a graphical representation based on a T–R²⁺–Si diagram. *European Journal of Mineralogy* **27**(5), 617–626.
- Brimhall GH and Crerar, DA** (1987) Ore fluids, Magmatic to supergene. In *Thermodynamic Modeling of Geologic Materials. Minerals, Fluids, and Melts* (eds ISE Carmichael & HP Eugster), 17, pp 235–321. Reviews in Mineralogy, Mineralogical Society of America, USA.
- Canil D and Lacourse T** (2020) Geothermometry using minor and trace elements in igneous and hydrothermal magnetite. *Chemical Geology* **541**, 119576.
- Cathelineau M** (1988) Cation site occupancy in chlorites and illites as a function of temperature. *Clay Minerals* **23**(4), 471–485.
- Cathelineau M and Nieva D** (1985) A chlorite solid solution geothermometer the Los Azufres (Mexico) geothermal system. *Contributions to Mineralogy and Petrology* **91**, 235–244.
- Celis A** (2015) Titanite as an indicator mineral for alkalic Cu-Au porphyry deposits in South central British Columbia. PhD Thesis, University of British Columbia, Vancouver, BC, Canada.
- Chauvet A** (2019) Structural control of ore deposits, The role of pre-existing structures on the formation of mineralised vein systems. *Minerals* **9**(1), 56.
- Chayes F** (1955) Potash feldspar as a by-product of the biotite-chlorite transformation. *The Journal of Geology* **63**, 75–82.
- Cho M and Liou JG** (1987) Prehnite–pumpellyite to greenschist facies transition in the Karmutsen metabasites, Vancouver Island, BC. *Journal of Petrology* **28**(3), 417–443.
- Cooke DR, Baker M, Hollings P, Sweet G, Chang Z, Danyushevsky L, Gilbert S, Zhou T, White N, Gemmel BJ and Inglis S** (2014) New advances in detecting the distal geochemical footprints of porphyry systems — epidote mineral chemistry as a tool for vectoring and fertility assessments. In *Society of Economic Geologists, Special Publication* **18**, 127–152.
- Cunningham CG** (1978) Pressure gradients and boiling as mechanisms for localizing ore in porphyry systems. *Journal of Research of the U.S Geological Survey* **6**, 745–754.
- Czamanske GK, Force ER and Moore WJ** (1981) Some geologic and potential resource aspects of rutile in porphyry copper deposits. *Economic Geology* **76**, 2240–2246.
- Davis GH, Reynolds SJ and Kluth CF** (2012) *Structural Geology of Rocks and Regions*. 3rd ed John Wiley & Sons, New York.
- Deditius AP, Reich M, Simon AC, Suvorova A, Knipping J, Roberts MP, Rubanov S, Dodd A and Saunders M** (2018) Nanogeochemistry of hydrothermal magnetite. *Contributions to Mineralogy and Petrology* **173**, 1–20.
- Deer WA, Howie RA and Zussman J** (1992) *An Introduction to the Rock-Forming Minerals*, 2nd, edition. Longman Scientific and Technical, London, UK, 696 pp.
- Deshmukh T, Prabhakar N, Bhattacharya A and Madhavan K** (2017) Late paleoproterozoic clockwise P-T history of the mahakoshal belt, central indian tectonic zone, implications for Columbia supercontinent assembly. *Precambrian Research* **298**, 56–78.
- Devarajan MK, Hanuma Prasad M, Prasad AVK and Soni MK** (1998) Gold mineralization in the Mahakoshal belt, Central India, a preliminary study. *Journal of the Geological Society of India* **52**, 147–152.
- Dilles JH** (1987) Petrology of the Yerington Batholith, Nevada; Evidence for evolution of porphyry copper ore fluids. *Economic Geology* **82**, 1750–1789.
- Dingwell DB and Brearley M** (1985) Mineral chemistry of igneous melanite garnets from analcite-bearing volcanic rocks, Alberta, Canada. *Contributions to Mineralogy and Petrology* **90**(1), 29–35.
- Eggleton RA and Banfield JF** (1985) The alteration of granitic biotite to chlorite. *American Mineralogist* **70**(9–10), 902–910.
- Essene EJ** (2009) Thermobarometry gone astray. In *Physics and Chemistry of Earth's Interior* (eds A K Gupta & S Dasgupta), pp. 101–133. Platinum Jubilee, Indian National Science Academy, SpringerVerlag, Berlin.
- Essene EJ and Peacor DR** (1995) Clay mineral thermometry — a critical perspective. *Clays and Clay Minerals* **43**, 540–553.
- Esteban JJ, Cuevas J, Tubía JM, Liati A, Seward D and Gebauer D** (2007) Timing and origin of zircon-bearing chlorite schists in the Ronda peridotites (Betic Cordilleras, Southern Spain). *Lithos* **99**(1–2), 121–135.
- Foster** (1960) Interpretation of the composition of trioctahedral micas. U S Geological Survey Professional Paper 354-B, 11–46.
- Franz G and Liebscher A** (2004) Physical and chemical properties of the epidote minerals – an introduction. *Reviews in Mineralogy and Geochemistry* **56**(1), 1–81.
- Geological Survey of India** (2001) *Mineral Atlas of India*. Geological Survey of India, Kolkata.
- Gieré R** (1986) Zirconolite, allanite and hoegbomite in a marble skarn from the Bergell contact aureole, implications for mobility of Ti, Zr and REE. *Contributions to Mineralogy and Petrology* **93**, 459–470.
- Giggenbach W F** (1997) The origin and evolution of fluids in magmatic-hydrothermal systems. In *Geochemistry of Hydrothermal Ore Deposits* (ed HL Barnes), pp. 737–796. 3rd edition, John Wiley and Sons, New York.
- Gillis KM, Muehlenbachs K, Stewart M, Gleeson T and Karson J** (2001) Fluid flow patterns in fast spreading East Pacific rise crust exposed at hess deep. *Journal of Geophysical Research, Solid Earth* **106**(B11), 26311–26329.
- Goldstein R H and Reynolds T J** (1994) Systematics of fluid inclusions in diagenetic minerals. Society for Sedimentary Geology Short Course 31.
- Hawthorne FC, Oberti R, Harlow GE, Maresch WV, Martin RF, Schumacher, JC and Welch MD** (2012) Nomenclature of the amphibole supergroup. *American Mineralogist* **97**(11–12), 2031–2048.

- Henley RW** (1985) The geothermal framework of epithermal deposits. In *Geology and Geochemistry of Epithermal Systems* (eds Berger BR & Bethke PM), pp. 1–24. Reviews in Economic Geology, Volume 2.
- Hillier S and Velde B** (1991) Octahedral occupancy and the chemical composition of diagenetic (low- temperature) chlorites. *Clay Mineral* **26**, 149–168.
- Huggins FE, Virgo D and Huckenholz HG** (1977) Titanium containing silicate garnets II, the crystal chemistry of melanites and schorlornites. *American Mineralogist* **62**, 646–665.
- Ilton ES and Eugster HP** (1989) Base metal exchange between magnetite and a chloride-rich hydrothermal fluid. *Geochimica et Cosmochimica Acta* **53**(2), 291–301.
- Inoue A** (1995) Formation of clay minerals in hydrothermal environments. In *Origin and Mineralogy of Clays: Clays and the Environment*, 268–329.
- Inoue A, Inoué S and Utada M** (2018) Application of chlorite thermometry to estimation of formation temperature and redox conditions. *Clay Minerals* **53**(2), 143–158.
- Inoue A, Kurokawa K and Hatta T** (2010) Application of chlorite geothermometry to hydrothermal alteration in Toyoha geothermal system, Southwestern Hokkaido, Japan. *Resource Geology* **60**, 52–70.
- Jébrak M** (1997) Hydrothermal breccias in vein-type ore deposits, a review of mechanisms, morphology and size distribution. *Ore Geology Reviews* **12**, 111–134.
- Jenkins DM and Bozhilov KN** (2003) Stability and thermodynamic properties of ferro-actinolite: a re-investigation. *American Journal of Science* **303**(8), 723–752.
- Jiang SY, Wang RC, Xu XS and Zhao KD** (2005) Mobility of high field strength elements (HFSE) in magmatic, metamorphic, and submarine hydrothermal systems. *Physics and Chemistry of the Earth, Parts A/B/C* **30**(17–18), 1020–1029.
- Jiang WT and Peacor DR** (1994) Formation of corrensite, chlorite and chlorite-mica stacks by replacement of detrital biotite in low-grade pelitic rocks. *Journal of Metamorphic Geology* **12**(6), 867–884.
- Jowett EC** (1991) Fitting iron and magnesium into the hydrothermal chlorite geothermometer. In GAC/MAC/SEG Joint Annual Meeting, Toronto, May 27–29, 1991, Program with Abstracts 16.
- Klein EL, Harris C, Giret A and Moura CA** (2007) The Cipoeiro gold deposit, Gurupi Belt, Brazil: Geology, chlorite geochemistry, and stable isotope study. *Journal of South American Earth Sciences* **23**(2–3), 242–255.
- Kowallis BJ, Christiansen EH, Dorais MJ, Winkel A, Henze P, Franzen L and Mosher H** (2022) Variation of Fe, Al, and F substitution in titanite (sphene). *Geosciences* **12**(6), 229.
- Laverne C, Vanko DA, Tartarotti P and Alt JC** (1995) Chemistry and geothermometry of secondary minerals from the deep sheeted dike complex, Hole 504B. In *Proceedings of the Ocean Drilling Program, Scientific Results* (eds, J Erzinger, K Becker, HJB Dick & LB Stokking), pp 167–190. volume 137–140.
- Leake BE, Woolley AR, Arps CE, Birch WD, Gilbert MC, Grice JD, Hawthorne FC, Kato A, Kisch HJ, Krivovichev VG and Linthout K** (1997) Nomenclature of amphiboles; report of the subcommittee on amphiboles of the international mineralogical association commission on new minerals and mineral names. *Mineralogical Magazine* **61**(405), 295–310.
- Liao Y, Wei C and Rehman HU** (2021) Titanium in calcium amphibole: behaviour and thermometry. *American Mineralogist* **106**(2), 180–191.
- Ling XX, Schmädicke E, Li QL, Gose J, Wu RH, Wang SQ, Liu Y, Tang GQ and Li XH** (2015) Age determination of nephrite by in-situ SIMS U-Pb dating syngenetic titanite: a case study of the nephrite deposit from Luanchuan, Henan, China. *Lithos* **220**, 289–299.
- LOBATO L M, Vieira F W R, Ribeiro-Rodrigues L C, Pereira LMM, Menezes MG, Junqueira PA and Pereira SLM** (1998) Styles of hydrothermal alteration and gold mineralization associated with the Nova Lima group of the Quadrilátero Ferrífero: Part II, the Archean mesothermal gold-bearing hydrothermal system. *Revista Brasileira de Geociências* **28**(3), 355–366.
- Lonker SW, Fitz Gerald JD, Hedenquist JW and Walshe JL** (1990) Mineral-fluid interactions in the Broadlands-Ohaaki Geothermal system, New Zealand. *American Journal of Science* **290**, 995–1068.
- Lovering TG** (1962) The origin of jasperoid in limestone. *Economic Geology* **57**(6), 861–889.
- Mikucki EJ and Ridley JR** (1993) The hydrothermal fluid of Archaean lode-gold deposits at different metamorphic grades, compositional constraints from ore and wall rock alteration assemblages. *Mineralium Deposita* **28**(6), 469–481.
- Mountain BW and Seward TM** (2003) Hydrosulfide/sulfide complexes of copper (I), Experimental confirmation of the stoichiometry and stability of Cu(HS)²⁻ to elevated temperatures. *Geochimica et Cosmochimica Acta* **67**, 3005–3014.
- Moura MA, Botelho NF, Olivo GR and Kyser TK** (2006) Granite-related Paleoproterozoic, Serrinha gold deposit, Southern Amazonia, Brazil: hydrothermal alteration, fluid inclusion and stable isotope constraints on genesis and evolution. *Economic Geology* **101**(3), 585–605.
- Nadol P, Angerer T, Mauk JL, French D and Walshe J** (2014) The chemistry of hydrothermal magnetite: a review. *Ore Geology Reviews* **61**, 1–32.
- Nair, K, Jain S and Yedekar D** (1995) Stratigraphy, structure and geochemistry of the Mahakoshal greenstone belt. *Memoir of the Geological Society of India* **37**, 403–432.
- Pacey A, Wilkinson JJ, Boyce AJ and Millar IL** (2020) Magmatic fluids implicated in the formation of propylitic alteration: oxygen, hydrogen, and strontium isotope constraints from the northparkes Porphyry Cu-Au district, New South Wales, Australia. *Economic Geology* **115**(4), 729–748.
- Pirajno F** (2009) Hydrothermal processes and wall rock alteration. In *Hydrothermal Processes and Mineral Systems* (ed F Pirajno) pp 73–164. Dordrecht, Springer.
- Pouchou JL and Pichoi F** (1988) A simplified version of the “PAP” model for matrix corrections in EPMA. Microbeam analysis, 315–318.
- Proffett JM** (2003) Geology of the Bajo de la Alumbrera porphyry copper-gold deposit, Argentina. *Economic Geology* **98**, 1535–1574.
- Rabbia OM, Hernández LB, French DH, King RW and Ayers JC** (2009) The El Teniente porphyry Cu-Mo deposit from a hydrothermal rutile perspective. *Mineralium Deposita* **44**, 849–866.
- Radhakrishna BP** (1989). Suspect tectono-stratigraphic terrane elements in the Indian subcontinent. *Journal Geological Society of India* **34**, 1–24.
- Reed MH** (1997) Hydrothermal alteration and its relationship to ore fluid composition. In *Geochemistry of Hydrothermal Ore Deposits* (ed HL Barnes), pp. 303–365. New York, John Wiley & Sons.
- Richards JP** (2011) Magmatic to hydrothermal metal fluxes in convergent and collided margins. *Ore Geology Reviews* **40**, 1–26.
- Robb L** (2005) *Introduction to Ore-Forming Processes*. Blackwell Publishing Company, Oxford. 239.
- Ronghua ZHANG, Shumin HU and Yanfeng SU** (2002) Hydrothermal alteration zoning and kinetic process of mineral-water interactions. *Acta Geologica Sinica* **76**(3), 351–366.
- Rose AW and Burt DM** (1979) Hydrothermal alteration. In *Geochemistry of Hydrothermal Ore Deposits* (ed HL Barnes), pp 173–235. 2nd edition, New York, John Wiley & Sons.
- Roy A and Bandyopadhyay B** (1990) Tectonic and structural pattern of the Mahakoshal belt of central India: a discussion. *Geological Survey of India, Miscellaneous Publication* **28**, 226–240.
- Roy A and Devarajan MK** (2000) A reappraisal of the stratigraphy and tectonics of the Palaeoproterozoic Mahakoshal supracrustal belt, Central India. *Geological Survey of India, Special Publication* **57**, 79–97.
- Roy A and Prasad MH** (2003) Tectonothermal events in Central Indian Tectonic Zone (CITZ) and its implications in Rodinian crustal assembly. *Journal of Asian Earth Science* **22** (2), 115–129.
- Seedorff E, Dilles JH, Proffett JM, Einaudi MT, Zurcher L, Stavast WJA, Johnson DA and Barton MD** (2005) Porphyry deposits, characteristics and origin of hypogene features *Economic Geology* **100**, 251–298.
- Seo JH, Guillong M and Heinrich CA** (2009) The role of sulphur in the formation of magmatic- hydrothermal copper-gold deposits. *Earth and Planetary Science Letters* **282**, 323–328.
- Sharma A, Das K, Chakraborty P, Shiraishi F and Kayama M** (2022) U–Pb zircon geochronology of a pyroclastic rock from the parsoi formation, Mahakoshal group, implications towards age and tectonics of the basin in Central Indian Tectonic Zone. *Geological Journal* **57**(10), 4122–4138. <https://doi.org/10.1017/S0016756825000056>
- Shepherd TJ, Rankin AH, Alderton DHM** (1985) *A Practical Guide to Fluid Inclusion Studies*. Blackie and Son, Glasgow. 239.

- Shikazono N and Kawahata H** (1987) Compositional differences in chlorite from hydrothermally altered rocks and hydrothermal ore deposits. *Canadian Mineralogist* **25**(3), 465–474.
- Shore M and Fowler AD** (1996) Oscillatory zoning in minerals; a common phenomenon. *Canadian Mineralogist* **34**(6), 1111–1126.
- Shriver NA and MacLean WH** (1993) Mass, volume and chemical changes in the alteration zone at the Norbec mine, Noranda, Quebec. *Mineralium Deposita* **28**, 157–166.
- Singhai RK and Singh AN** (2001) Exploration for gold, silver and basemetals in Imalia Block, Sleemanabad Area, Katni District, Madhya Pradesh (E1-Stage), Records of the Geological Survey of India, Volume 135, part (6), 82–83.
- Skinner BJ** (1997) Hydrothermal mineral deposits, what we do and don't know. In *Geochemistry of Hydrothermal Ore Deposits* (ed Barnes HL), pp. 1–29. New York, John Wiley & Sons Inc.
- Talusani RV** (2001). Possible Carlin-type disseminated gold mineralization in the Mahakoshal fold belt, central India. *Ore Geology Reviews* **17**(4), 241–247.
- Timpa S, Gillis KM and Canil D** (2005) Accretion-related metamorphism of the Metchosin igneous complex, southern Vancouver Island, British Columbia. *Canadian Journal of Earth Sciences* **42**(8), 1467–1479.
- Toplis MJ and Corgne A** (2002) An experimental study of element partitioning between magnetite, clinopyroxene and iron-bearing silicate liquids with particular emphasis on vanadium. *Contributions to Mineralogy and Petrology* **144**(1), 22–37.
- Torresi I, Xavier RP, Bortholoto DFA and Monteiro LVS** (2012) Hydrothermal alteration, fluid inclusions and stable isotope systematics of the Alvo 118 iron oxide – copper – gold deposit, Caraja's Mineral Province (Brazil): Implications for ore genesis. *Mineralium Deposita* **47**, 299–323.
- Tripathi S** (2008) Geological characterisation of the carbonate - hosted polymetallic prospect at Imalia, Mahakoshal belt, Central India. PhD thesis, University of Delhi, India.
- Tripathi S and Deb M** (2022) Mineralogy of the Imalia Au-Sn-bearing polymetallic sulfide deposit, Mahakoshal belt, Central India. *Journal of Asian Earth Sciences* **X** **8**, 100117.
- Walshe JL** (1986) A six-component chlorite solid solution model and the conditions of chlorite formation in hydrothermal and geothermal systems. *Economic Geology* **81**(3), 681–703.
- Wen G, Li JW, Hofstra AH, Koenig AE, Lowers HA and Adams D** (2017) Hydrothermal reequilibration of igneous magnetite in altered granitic plutons and its implications for magnetite classification schemes: Insights from the Handan-Xingtai iron district, North China Craton. *Geochimica et Cosmochimica Acta* **213**, 255–270.
- Wiewióra A and Weiss Z** (1990) Crystallochemical classifications of phyllosilicates based on the unified system of projection of chemical composition: II The chlorite group. *Clay Minerals* **25**(1), 83–92.
- Wones DR and Eugster HP** (1965) Stability of biotite: Experiment, theory, and application. *American Mineralogist* **50**, 1228–1272.
- Wu C, Chen H, Hong W, Li D, Liang P, Fang J, Zhang L and Lai C** (2019) Magnetite chemistry and implications for the magmatic-hydrothermal ore-forming process: an example from the Devonian Yuleken porphyry Cu system, NW China. *Chemical Geology* **522**, 1–15.
- Xiao B, Chen H, Hollings P, Zhang Y, Feng Y and Chen X** (2020) Chlorite alteration in porphyry Cu systems: New insights from mineralogy and mineral chemistry. *Applied Clay Science* **190**, 105585.
- Xiao B and Huayong C** (2020) Elemental behavior during chlorite alteration: new insights from a combined EMPA and LA-ICPMS study in porphyry Cu systems. *Chemical Geology* **543**, 119604.
- Xie F, Tang J, Lang X and Ma D** (2018) The different sources and petrogenesis of Jurassic intrusive rocks in the southern Lhasa subterranean, Tibet: Evidence from the trace element compositions of zircon, apatite and titanite. *Lithos* **314**, 447–462.
- Xie XG, Byerly GR and Ferrell Jr RE** (1997) Ilb trioctahedral chlorite from the Barberton greenstone belt: Crystal structure and rock composition constraints with implications to geothermometry. *Contributions to Mineralogy and Petrology* **126**, 275–291.
- Yavuz F** (2003) Evaluating micas in petrologic and metallogenic aspect, Part II-Applications using the computer program Mica. *Computers and Geosciences* **29**(10), 1203–1213.
- Yedekar DB, Jain SC, Nair K.K.K and Dutta KK** (1990). The Central Indian Collision Suture. Geological Survey of India, Special Publication No. 28, 1–43.
- Yuan H, Shen P and Pan H** (2018) Nature and evolution of hydrothermal fluids in the Formation of the Tuwu porphyry copper deposit in the Eastern Tianshan Mountains, NW China. *Journal of Asian Earth Science* **165**, 210–227.
- Yuguchi T, Sasao E, Ishibashi M and Nishiyama T** (2015) Hydrothermal chloritization processes from biotite in the Toki granite, Central Japan: Temporal variations of the compositions of hydrothermal fluids associated with chloritization. *American Mineralogist* **100**(5-6), 1134–1152.
- Zane A and Weiss Z** (1998) A procedure for classifying rock-forming chlorites based on microprobe data. *Atti della Accademia Nazionale dei Lincei. Rendiconti. Scienze Fisiche e Naturali* **9**(1), 51–56.
- Zang W and Fyfe WS** (1995) Chloritization of the hydrothermally altered bedrock at the Igarapé Bahia gold deposit, Carajás, Brazil. *Mineralium Deposita* **30**, 30–38
- Zhang S, Xiao B, Long X, Chu G, Cheng J, Zhang Y and Xu G** (2020) Chlorite as an exploration indicator for concealed skarn mineralization: Perspective from the Tonglushan Cu–Au–Fe skarn deposit, Eastern China. *Ore Geology Reviews* **126**, 103778.